

# On the measurement of $S_{\text{diff}}$ splitting caused by lowermost mantle anisotropy

Jonathan Wolf<sup>1,\*</sup>, Maureen D. Long<sup>1</sup>, Neala Creasy<sup>2,3</sup>, Edward Garnero<sup>4</sup>

---

## Abstract

Seismic anisotropy has been detected at many depths of the Earth, including its upper layers, the lowermost mantle, and the inner core. While upper mantle seismic anisotropy is relatively straightforward to resolve, lowermost mantle anisotropy has proven to be more complicated to measure. Due to their long, horizontal raypaths along the core-mantle boundary, S waves diffracted along the core-mantle boundary ( $S_{\text{diff}}$ ) are potentially strongly influenced by lowermost mantle anisotropy.  $S_{\text{diff}}$  waves can be recorded over a large epicentral distance range and thus sample the lowermost mantle everywhere around the globe.  $S_{\text{diff}}$  therefore represents a promising phase for studying lowermost mantle anisotropy; however, previous studies have pointed out some difficulties with the interpretation of differential  $SH_{\text{diff}}-SV_{\text{diff}}$  travel times in terms of seismic anisotropy. Here, we provide a new, comprehensive assessment of the usability of  $S_{\text{diff}}$  waves to infer lowermost mantle anisotropy. Using both axisymmetric and fully 3D global wavefield simulations, we show that there are cases in which  $S_{\text{diff}}$  can reliably detect and characterize deep mantle anisotropy when measuring traditional splitting parameters (as opposed to differential travel times). First, we analyze isotropic effects on  $S_{\text{diff}}$  polarizations, including the influence of realistic velocity structure (such as 3D velocity heterogeneity and ultra-low velocity zones), the character of the lowermost mantle velocity gradient, mantle attenuation structure, and Earth's Coriolis force. Second, we evaluate effects of seismic anisotropy in both the upper and the lowermost mantle on  $SH_{\text{diff}}$  waves. In particular, we investigate how  $SH_{\text{diff}}$  waves are split by seismic anisotropy in the upper mantle near the source and how this anisotropic signature propagates to the receiver for a variety of lowermost mantle models. We demonstrate that, in particular and predictable cases, anisotropy leads to  $S_{\text{diff}}$  splitting that can be clearly distinguished from other waveform effects. These results enable us to lay out a

---

\*Corresponding author

*Email address:* [jonathan.wolf@yale.edu](mailto:jonathan.wolf@yale.edu) (Jonathan Wolf)

<sup>1</sup>Department of Earth and Planetary Sciences, Yale University, New Haven, CT, USA

<sup>2</sup>Los Alamos National Laboratory, Los Alamos, NM, USA

<sup>3</sup>Colorado School of Mines, Golden, CO, United States

<sup>4</sup>School of Earth and Space Exploration, Arizona State University, Tempe, AZ, USA

strategy for the analysis of  $S_{\text{diff}}$  splitting due to anisotropy at the base of the mantle, which includes steps to help avoid potential pitfalls, with attention paid to the initial polarization of  $S_{\text{diff}}$  and the influence of source-side anisotropy. We demonstrate our  $S_{\text{diff}}$  splitting method using three earthquakes that occurred beneath the Celebes Sea, measured at many Transportable Array (TA) stations at a suitable epicentral distance. We resolve consistent and well-constrained  $S_{\text{diff}}$  splitting parameters due to lowermost mantle anisotropy beneath the northeastern Pacific Ocean.

Keywords: Planetary interiors, Numerical modelling, Computational seismology, Seismic anisotropy, Wave propagation

---

## 1. Introduction

Seismic anisotropy, or the directional dependence of seismic wave speeds, typically results from deformation in the Earth (e.g., Long and Becker, 2010). Seismic anisotropy has been identified in the crust (e.g., Barruol and Kern, 1996; Erdman et al., 2013), the upper mantle (e.g., Silver, 1996; Chang et al., 2014), the mantle transition zone (e.g., Yuan and Beghein, 2014; Chang and Ferreira, 2019) and Earth's inner core (e.g., Romanowicz et al., 2016; Frost et al., 2021). The bulk of the lower mantle is largely isotropic (e.g., Panning and Romanowicz, 2006), but some studies have suggested seismic anisotropy in the uppermost lower mantle, particularly in subduction zones (e.g., Foley and Long, 2011; Lynner and Long, 2015; Mohiuddin et al., 2015; Ferreira et al., 2019). Finally, the bottom 200-300 km of the mantle, in the following synonymously referred to as  $D''$ , has been shown to be anisotropic in many places (e.g., Lay et al., 1998; Garnero et al., 2004; Wookey et al., 2005; Nowacki et al., 2010; Creasy et al., 2017; Lutz et al., 2020; Wolf and Long, 2022; Wolf et al., 2022). A main cause for seismic anisotropy is the preferential alignment of intrinsically anisotropic minerals due to mantle flow (e.g., Nowacki et al., 2011; Karato et al., 2008).

As with the upper mantle, measurements of lowermost mantle anisotropy can potentially resolve deep mantle deformation and map patterns of flow at the base of the mantle. In practice, however, such inferences remain challenging to make. These difficulties reflect shortcomings or assumptions in commonly used measurements methods (e.g., Nowacki and Wookey, 2016; Wolf et al., 2022a), limitations in data coverage (e.g., Ford et al., 2015; Creasy et al., 2017; Wolf et al., 2019), and/or uncertainties about realistic lowermost mantle elasticity scenarios (e.g., Nowacki et al., 2011; Creasy et al., 2020). For instance, even with perfect knowledge about potential elastic tensors describing lowermost mantle materials, seismic anisotropy must generally be measured from multiple directions to uniquely constrain deformation and mineralogy (e.g., Nowacki et al., 2011; Creasy et al., 2019). The deep mantle is likely dominantly composed of bridgmanite or its high-pressure polymorph

post-perovskite, along with ferropericlase; the single-crystal elasticity and dominant slip systems of the minerals at the relevant pressure-temperature conditions are not precisely known (e.g., Creasy et al., 2020). Therefore, it is not completely straightforward to infer deformation geometry from measured shear wave splitting parameters (fast polarization directions and delay times). One strategy is to assume a plausible lowermost mantle composition based on the likely temperature conditions and seismic velocities of a certain region and carry out forward modelling to make predictions that can be compared to observations (e.g., Nowacki et al., 2010; Ford et al., 2015; Creasy et al., 2021; Wolf and Long, 2022).

Recent progress in full-wave modelling of seismic anisotropy with arbitrary geometries in the lowermost mantle has led to an improved understanding of the shortcomings inherent in commonly used shear wave splitting measurement techniques (Nowacki and Wookey, 2016; Tesoniero et al., 2020; Wolf et al., 2022a; 2022b), which are typically based on ray theory (a high-frequency approximation to the wave equation). However, not all of the difficulties have successfully been resolved, and challenges remain with commonly used measurement methods such as differential S-ScS and SKS-SKKS splitting. Thus, it is important to explore alternatives to the commonly used seismic phases for measuring  $D''$  anisotropy, and to validate them using full-wave simulations rather than relying solely on ray-theoretical assumptions. A viable candidate phase for  $D''$  anisotropy measurements is the  $S_{\text{diff}}$  phase, because of its particularly long and horizontal raypaths along the CMB (Figure 1a), along which it can accumulate splitting. However, extracting information about deep mantle anisotropy from  $S_{\text{diff}}$  waveforms is non-trivial. This is partly because  $S_{\text{diff}}$  waves are generally neither perfectly SH nor SV polarized in absence of anisotropy; furthermore,  $SH_{\text{diff}}$  and  $SV_{\text{diff}}$  can accumulate a time shift due to isotropic structure (e.g., Komatitsch et al., 2010; Borgeaud et al.; 2016; Parisi et al., 2018), which can potentially be misinterpreted as shear wave splitting. Further, it must be ensured that phase interference is not misinterpreted as splitting (Komatitsch et al., 2010; Borgeaud et al.; 2016; Parisi et al., 2018). Another challenge is that the splitting signature of  $S_{\text{diff}}$  reflects the integrated effects of seismic anisotropy along the raypath, including the source and receiver side upper mantle as well as  $D''$ .

Despite these challenges, the interpretation of  $S_{\text{diff}}$  splitting in terms of lowermost mantle anisotropy has a substantial history (e.g., Vinnik et al., 1989; 1995; 1998a; 1998b; Garnero and Lay, 1997; Ritsema et al., 1998; Fouch et al., 2001). In some early papers,  $S_{\text{diff}}$  splitting was compared to the splitting of SK(K)S waves to assess the upper mantle anisotropy contribution to the waveforms, often under the assumption that  $SV_{\text{diff}}$  should have died off after travelling a certain epicentral distance, typically  $110^\circ$  (e.g., Vinnik et al., 1989). Alternatively, some studies have focused on the time delay between  $SH_{\text{diff}}$  and  $SV_{\text{diff}}$  without

explicitly measuring splitting parameters (e.g., Ritsema et al., 1998; Fouch et al., 2001). While  $S_{\text{diff}}$  waves are in fact often primarily SH-polarized, recent work has shown that the assumption that  $SV_{\text{diff}}$  has completely died off at  $110^\circ$  distance cannot always be made (Komatitsch et al., 2010; Borgeaud et al., 2016). It has also been shown that the SH and SV components of S and  $S_{\text{diff}}$  (Komatitsch et al., 2010; Borgeaud et al., 2016; Parisi et al., 2018) can accumulate an apparent time-shift that can potentially mimic splitting, even for isotropic Earth models. As a result, it has recently become less common to measure  $D''$  seismic anisotropy using  $S_{\text{diff}}$ . A few exceptions (Cottaar and Romanowicz, 2013; Wolf and Long, 2022) have typically relied on specific arguments about likely initial polarizations of the waves under study.

In this study, we provide a new and comprehensive examination of the suitability of  $S_{\text{diff}}$  splitting measurements to infer lowermost mantle anisotropy using global wavefield modeling tools. We analyze potential pitfalls in  $S_{\text{diff}}$  splitting analysis, and develop strategies to avoid them. For this purpose, we complement previous studies from Tesoniero et al. (2020) and Wolf et al. (2022a,b), who have analyzed the accuracy of commonly used shear-wave splitting techniques for  $D''$  anisotropy studies with a focus on SK(K)S and S/ScS. We also complement a recent study by Creasy et al. (in review), who investigated the effects of the Earth's Coriolis force on SK(K)S polarizations. We undertake a similar approach as in these previous studies, using the `AxiSEM3D` (Leng et al., 2016, 2019) and `SPECFEM3D_GLOBE` (Komatitsch and Tromp, 2002a, 2002b) software to model global wave propagation.

In contrast to previous studies (Komatitsch et al., 2010; Borgeaud et al., 2016; Parisi et al., 2018) that used global wavefield simulations to examine  $S_{\text{diff}}$  waveform behavior, we do not explicitly investigate differential  $SH_{\text{diff}}-SV_{\text{diff}}$  travel times. Rather, we analyze how  $S_{\text{diff}}$  phases can be used to infer robust shear-wave splitting parameters (time delay, fast-axis polarization direction, and splitting intensity) associated with lowermost mantle anisotropy. Unlike the measurement of differential  $SH_{\text{diff}}-SV_{\text{diff}}$  travel times, such an analysis includes strict requirements for the shape of the waveform. Whenever we use the term  $S_{\text{diff}}$ -splitting in the following, we refer to the explicit measurement of splitting parameters and not to the analysis of time delays.

We conduct a suite of global wavefield simulations with increasing complexity to assess the conditions under which  $S_{\text{diff}}$  waves are suitable for shear wave splitting measurements. In the first set of simulations, we analyze the effects of realistic isotropic velocity structure on  $S_{\text{diff}}$  polarizations. In particular, we analyze the assumptions and conditions when  $SV_{\text{diff}}$  and  $SH_{\text{diff}}$  die off. While it has been shown that assumptions cannot always be made (Komatitsch et al., 2010), no study so far has assessed these assumptions comprehensively. We continue with simulations investigating the effects of realistic 3D velocity structure and

Earth's Coriolis force on  $S_{\text{diff}}$  polarizations. In a second set of simulations, we investigate the effect of seismic anisotropy on  $SH_{\text{diff}}$  waves in detail. We examine the conditions under which splitting caused by source-side anisotropy could potentially be misdiagnosed as showing evidence for lowermost mantle anisotropy. Furthermore, we analyze the limits of resolution for the cases in which  $S_{\text{diff}}$  splitting can indeed be reliably attributed to lowermost mantle anisotropy. This second set of simulations reveals how exactly  $D''$  anisotropy expresses itself in  $S_{\text{diff}}$  waveforms, particularly for cases in which there is also an upper mantle contribution. Finally, we use the insights gained for our  $S_{\text{diff}}$ -wavefield simulations to outline a novel strategy for using  $S_{\text{diff}}$  splitting measurements to reliably infer deep mantle anisotropy. We use these insights to conduct a thorough splitting analysis for three deep earthquakes that occurred in the Celebes Sea in 2009 and 2010, for which  $S_{\text{diff}}$  waves, recorded at a large swath of stations across USArray, sample the lowermost mantle beneath the northeastern Pacific Ocean.

## 2. Methods

### 2.1. Full-wave simulations

AxiSEM3D and SPECFEM3D\_GLOBE are two commonly used tools to conduct global wavefield simulations. In this work, we primarily use AxiSEM3D due to its computational efficiency, which allows us to calculate synthetic seismograms down to periods that are commonly used for shear wave splitting measurements ( $\sim 5$  s). For these calculations, we extend the work of Tesoniero et al. (2020) and Wolf et al. (2022a,b), who have established AxiSEM3D as a suitable tool to conduct full-wave simulations for models that include anisotropy of arbitrary symmetry. To investigate the effects of Earth's Coriolis force, we calculate seismograms down to  $\sim 9$  s using SPECFEM3D\_GLOBE, extending work from Creasy et al. (in review). The Coriolis force effect on body waves is frequency dependent, but because the period we are using in our SPECFEM3D\_GLOBE simulations (9 s) is much smaller than the period of Earth's rotation, the results would be unaffected if we were to calculate synthetics for lower periods (Snieder et al., 2016). SPECFEM3D\_GLOBE gives the user the option to calculate synthetics with and without considering Earth's rotation.

The initial input model for our numerical simulations with AxiSEM3D and SPECFEM3D\_GLOBE is isotropic PREM (Dziewonski and Anderson, 1981). All simulations include attenuation and ellipticity. Building on this simple scenario, we move towards increasingly complex models in our AxiSEM3D simulations. To do so, we replace the initial PREM input model at certain depths with different or more complex structure. Specifically, we first replace lowermost mantle properties (e.g, velocity, velocity-gradient,  $Q_\mu$ ) in the context of an isotropic Earth to investigate the influence of various factors on how SH and SV amplitudes die off as

a function of distance for diffracted waves. We also run simulations for a model that replaces PREM with 3D tomographic models to assess the influence of 3D velocity heterogeneity on  $S_{\text{diff}}$  polarizations. Next, we shift our attention to simulations that include seismic anisotropy, in particular source-side and lowermost mantle anisotropy, for background models based on both PREM and PREM+3D tomographic model.

To identify the effects of Earth’s rotation on  $S_{\text{diff}}$  polarizations, we conduct simulations with SPECSEM3D\_GLOBE. In this solver, the globe is divided into six chunks; we apply 480 spectral elements along one side of each chunk at the surface, resolving down to a minimum period of  $\sim 9$  s during simulations. We conduct two simulations including gravity (Cowling approximation) and the ocean load (Komatitsch and Tromp, 2002b), one including Earth’s rotation and the other excluding it. The source, at 616 km depth, is selected from the Global Centroid-Moment-Tensor catalogue (Ekström et al., 2012; event name: 201004112208A), but we change the source location to  $25^\circ\text{S}$  and  $66^\circ\text{W}$ . This event is selected so that the north-south propagation directions are far from the nodal planes of the source, to amplify the rotation effect (Creasy et al., in review). More than 1,000 pseudo receivers are placed across the global mesh with  $8^\circ$  - spacing. Waveforms from the simulations are bandpass filtered to retain energy between 10 – 50 s before processing.

An example of a typical source-receiver configuration used for our synthetic simulations with AxiSEM3D is shown in Figure 1b. Here, we place our source and receivers along the equator. The source is chosen to be at longitude  $-90^\circ$  and the receivers are placed along the equator at epicentral distances between  $103 - 130^\circ$ . For this scenario, we choose a focal depth of 500 km and a moment tensor whose only non-zero component is  $M_{tp}$  for perfect initial SH polarization. The same is done for perfect initial SV polarization (keeping  $M_{tt}$  as the only non-zero component). The details of the moment tensor are only relevant insofar as they affect the initial polarization of the wave; we choose these simple moment tensor scenarios because they are straightforward to understand and interpret. An additional source-receiver configuration that we use is an equivalent scenario along the zero meridian with the source at the north pole and a focal depth of 0 km. These two configurations are arbitrary, but they allow us to build on results from an initial benchmarking exercise without having to rerun computationally expensive simulations for another source-receiver setup. We use the first configuration (shown in Figure 1b) for all the isotropic AxiSEM3D simulations (Section 3) and the alternative configuration for all simulations that include lowermost mantle anisotropy (Section 4).

For simulations that include anisotropy near the source, we incorporate a 200 km thick layer with horizontally transversely isotropic (HTI) symmetry. We calculate appropriate elastic tensors using MSAT (Walker and Wookey, 2012), creating an elastic tensor at each

depth increment whose isotropic average matches isotropic PREM velocities. We tune the elastic tensor using MSAT to have an anisotropic strength of either 2% or 4%. We incorporate a source-side anisotropy layer at a depth range of 30 – 230 km for simulations with a source depth of 0 km, and at a depth range of 500 – 700 km for a focal depth of 500 km. In both cases the raypath through the layer is sufficiently vertical that the effects of focal depth and anisotropic layer depth on the observed splitting are minor. Whenever we include upper mantle anisotropy, we make sure that the HTI tensor is rotated such that its fast direction is at an angle of  $45^\circ$  with respect to the polarization of the wave, which maximizes splitting.

For the lowermost mantle, we use an elastic tensor based on textured post-perovskite (Ppv) from the elastic tensor library of Creasy et al. (2020), for simple shear with 100% strain. This tensor incorporates estimates of single-crystal elasticity from Stackhouse et al. (2005) and is based on a model of texture development using a viscoplastic selfconsistent modeling approach (Creasy et al., 2020). We rotate this tensor appropriately to obtain strong  $S_{\text{diff}}$  splitting, following Wolf et al. (2022b). For the cases for which we measure splitting intensities (Section 4), we mix this Ppv tensor with its isotropic equivalent (using MSAT) to obtain an anisotropic strength that is only 1/3 of the original tensor. This allows us to obtain more realistic splitting intensities ( $\sim 1$ ; Section 2.2) at the receiver when using a global, uniform layer of anisotropy. In the real Earth, of course, some regions of  $D''$  may be strongly anisotropic while others are isotropic. We emphasize that while we focus on a Ppv anisotropy scenario in these simulations, our conclusions are more general and do not depend on the details a certain elasticity scenario. Unless specified otherwise, the thickness of the anisotropic basal mantle layer that we incorporate into our simulations is 150 km, following previous work (Wolf et al., 2022a; 2022b).

## 2.2. Shear wave splitting measurements

A shear wave travelling through an anisotropic medium will split into two quasi-S wave components, one fast and one slow (e.g., Silver and Chan, 1991). These quasi-S waves will thus accumulate a time delay with respect to each other, usually referred to as  $\delta t$ . The fast direction of the anisotropic material is inferred by measuring the fast polarization direction of the wave, called  $\phi$ . The fast polarization direction,  $\phi$ , is usually measured as a (clockwise) azimuth from the north. In this study, we also use  $\phi'$ , which denotes the fast polarization direction measured clockwise from the backazimuthal direction (meaning that  $\phi$  is identical to  $\phi'$  if the backazimuth is  $0^\circ$ ; Nowacki et al., 2010). Another quantity that is very useful for studies of seismic anisotropy (in part due to its robustness in case of noise or weak splitting) is the splitting intensity, in the following abbreviated as  $SI$  (Chevrot, 2000). The typical definition of  $SI$  (for initially SV polarized waves) is

$$SI_{SV} = -2 \frac{T(t)R'(t)}{|R'(t)|^2} \approx \delta t \sin(2(\alpha - \phi)) , \quad (1)$$

with  $T(t)$  denoting the transverse component,  $R'(t)$  the time derivative of the radial component,  $\delta t$  the time lag between the fast and slow travelling quasi S-waves, and  $\alpha$  the polarization direction of the incoming wave (equivalent to the backazimuth for SKS waves following their exit from the core). Thus,  $SI$  values are large if the transverse component resembles the radial component time derivative (which is true in the case of splitting; Silver and Chan, 1991; Chevrot, 2000) and has a high amplitude. The definition in Equation (1) is usually used because splitting measurements are often made on \*KS phases that are initially SV polarized due to the P-to-SV conversion at the CMB. For  $SH_{\text{diff}}$  waves, we will use an alternate definition of  $SI$ :

$$SI_{SH} = -2 \frac{R(t)T'(t)}{|T'(t)|^2} , \quad (2)$$

where  $T'(t)$  denotes the transverse component time derivative. For these waves, when  $SH_{\text{diff}}$  undergoes splitting and some energy is partitioned into  $SV_{\text{diff}}$ , the transverse component time derivative will have the shape of the radial component.

We bandpass-filter our synthetic and real data before measuring splitting, typically retaining periods between 8–25 s (for the assessment of Coriolis effects we instead use 10–25 s). We conduct our splitting measurements on both synthetic and real data using a modified version of the MATLAB-based graphical user interface SplitRacer (Reiss and Rmpker, 2017; Reiss et al., 2019). This version of SplitRacer retrieves the splitting parameters ( $\phi$ ,  $\delta t$ ) using the transverse energy minimization approach (Silver and Chan, 1991), paired with the corrected error determination of Walsh et al. (2013); additionally, this version measures the splitting intensity. We modified SplitRacer slightly for this study, measuring  $\phi'$  instead of  $\phi$ , thus transforming  $\phi$  into the ray reference frame. We also switched the transverse and radial components to estimate  $S_{\text{diff}}$  splitting. We call the fast polarization direction obtained this way  $\phi''$ , which equals  $90^\circ - \phi'$ . This direction  $\phi''$  appears on many figures but will also always be translated into the  $\phi'$  coordinate frame.

### 3. Isotropic effects on $S_{\text{diff}}$ waveforms

#### 3.1. Influence of various lowermost mantle properties on $S_{\text{diff}}$ amplitudes

First, we investigate the influence that different isotropic lowermost mantle properties have on  $S_{\text{diff}}$  amplitudes, specifically on how  $S_{\text{diff}}$  amplitudes decrease as a function of distance in an isotropic Earth. Doornbos and Mondt (1979) and Komatitsch et al. (2010) have previously shown how  $S_{\text{diff}}$  amplitudes decrease with distance, and that the relative

SV/SH amplitude ratio decrease depends on lowermost mantle properties. Here, we extend this work and systematically examine the influence of a realistic range of lowermost mantle properties on the amplitude decay with distance of  $SH_{\text{diff}}$  and  $SV_{\text{diff}}$ . Our motivation is to identify whether it can be assumed, for different lowermost mantle structure and epicentral distance ranges, that  $SV_{\text{diff}}$  has died off while  $SH_{\text{diff}}$  has not. This assumption is important for  $S_{\text{diff}}$  splitting analyses, as many studies presume that  $SH_{\text{diff}}$  polarization energy dominates the  $S_{\text{diff}}$  signal, due to the assumed die-off of  $SV_{\text{diff}}$  polarization energy by a particular distance (e.g., Vinnik et al., 1989). While this assumption has been shown to be inadequate in some cases (Komatitsch et al., 2010; Borgeaud et al., 2016), it may be justified for some combinations of lowermost mantle conditions, which we interrogate here.

We show synthetic seismograms for the three scenarios shown in Figure 2. Scenario 1 incorporates isotropic PREM and for scenarios 2 and 3, lowermost mantle velocities are decreased or increased, respectively. In the Supplementary Information, we additionally show some scenarios with different lowermost mantle velocity gradients (Figure S1) and a changed lowermost mantle shear wave attenuation (Figure S2).

The results for scenario 1 (isotropic PREM) are shown in Figure 3 for different initial polarizations of the  $S_{\text{diff}}$  waves. We focus, in particular, on how radial and transverse amplitudes decrease as a function of distance. We observe little or no interfering energy from other phases in the transverse component record sections for the entire distance range, although for SV there is some non- $S_{\text{diff}}$  energy for larger distances. While this SV energy does not correspond to any standard phase, we speculate that it comes from reflecting energy in the upper layers of the PREM input model, a phenomenon that has been observed before for ScS (Wolf et al., 2022b). Both SV and SH amplitudes are significant at distances of  $130^\circ$ , although  $SV_{\text{diff}}$  appears to die off slightly faster than  $SH_{\text{diff}}$ . This simple simulation reinforces previous findings (Komatitsch et al., 2010; Borgeaud et al., 2016) that it is generally incorrect to assume that for an  $S_{\text{diff}}$  wave with arbitrary initial polarization, the initial  $SV_{\text{diff}}$  energy has died off at a particular distance, while  $SH_{\text{diff}}$  has not. We next extend on this scenario and examine how particular aspects of lowermost mantle structure affect  $SH_{\text{diff}}$  and  $SV_{\text{diff}}$  amplitudes.

We investigate the influence of reasonable velocity deviations (e.g., Simmons et al., 2010; French and Romanowicz, 2014) from PREM-like velocities, still in the context of 1D velocity profiles. We assume typical deviations of  $\sim \pm 2\%$  for LLVP regions and regions with higher velocities dominated by slab remnants, respectively. To have maximum radial and transverse amplitudes for visualization, we conduct two different end-member simulations, for initially solely SH and solely SV polarized  $S_{\text{diff}}$  waves, respectively. The waveforms for simulations that incorporate such a change in lowermost mantle velocity are displayed in record sections

in Figure 4, which uses similar plotting conventions as Figure 3. When velocities are higher than PREM,  $\text{SH}_{\text{diff}}$  and  $\text{SV}_{\text{diff}}$  amplitudes decrease similarly as a function of distance as for PREM. When velocities are lower than PREM, amplitudes decrease more slowly. While this is a general trend for both  $\text{SH}_{\text{diff}}$  and  $\text{SV}_{\text{diff}}$ , we find that  $\text{SV}_{\text{diff}}$  energy dies off faster than  $\text{SH}_{\text{diff}}$  for higher velocities, but behaves similarly as a function of distance for lower velocities (Figure 4). This implies that the assumption that initial  $\text{SV}_{\text{diff}}$  energy has died off at any particular distance, while  $\text{SH}_{\text{diff}}$  has not, will be more suitable (but still not perfect) for faster than average regions in the lowermost mantle. The details of how  $\text{SH}_{\text{diff}}$ - and  $\text{SV}_{\text{diff}}$  die off, however, do not only depend on absolute lowermost mantle velocities but also on the velocity gradient (Supplementary Figure S1). In Figure S1, we compare scenarios that incorporate a velocity jump with linear velocity gradients at the base of the mantle. For higher and lower velocities than average at the base of the mantle, a linear velocity gradient will lead to a sharper amplitude decrease with distance than a velocity jump.

We next show that the mantle shear quality factor can have an influence on the amplitude decrease of SH- and  $\text{SV}_{\text{diff}}$  waves.  $Q_\mu$  is usually assumed to have a value between 200 and 400 in radially symmetric models (e.g., Dziewonski and Anderson, 1981; Lawrence and Wysession, 2006), although there may be a substantial lateral variability (e.g., Romanowicz and Mitchell, 2007). To account for this, we test two relatively extreme cases with different  $Q_\mu$  values ( $Q_\mu = 75$  and  $Q_\mu = 1000$ ), leaving  $Q_\kappa$  unchanged. The results for both cases are shown in Supplementary Figure S2. Changing  $Q_\mu$  appears to have a larger influence on  $\text{SV}_{\text{diff}}$  than  $\text{SH}_{\text{diff}}$ . While the details likely reflect the specific details of the implemented  $Q_\mu$  model, in general this implies that the propagation of initial  $\text{SV}_{\text{diff}}$  energy will not only depend on the details of the lowermost mantle velocity and velocity gradient, but also on  $Q_\mu$ . This agrees with results from Borgeaud et al. (2016), who investigated the dependence of apparent  $\text{SH}_{\text{diff}}$ - $\text{SV}_{\text{diff}}$  differential times on lowermost mantle  $Q_\mu$  structure in detail.

These simulations show that, although  $\text{SV}_{\text{diff}}$  dies off faster than  $\text{SH}_{\text{diff}}$  in most cases, a blanket assumption that  $\text{SV}_{\text{diff}}$  dies off at a specific epicentral distance is unwarranted. This is important because if SV energy is present for  $\text{S}_{\text{diff}}$  in absence of anisotropy, then isotropic waveform effects can potentially be mistaken for splitting, even for isotropic Earth models. For instance, Komatitsch et al. (2010), Borgeaud et al. (2016) and Parisi et al. (2018) showed that isotropic structure can lead to a relative time-shift between  $\text{SH}_{\text{diff}}$  and  $\text{SV}_{\text{diff}}$  components (although the authors did not explicitly measure splitting). Our results imply that  $\text{S}_{\text{diff}}$  waves can be used for shear wave splitting measurements only if it can be established that, for a given event and raypath and in absence of lowermost mantle anisotropy, the  $\text{SV}_{\text{diff}}$  component is expected to be negligible. This means that whether a given measurement is usable will depend on the initial polarization of the wave as well as the

lowermost mantle structure. This criterion can be evaluated through synthetic modelling. In practice, many  $S_{\text{diff}}$  waves will in fact be suitable for splitting analysis. Therefore, direct S and ScS become asymptotic as they eventually become the same wave at the diffraction distance. Their SV polarities, however, are opposite, resulting in destructive interference; depending on the velocity structure, this can result in a rapidly diminishing  $SV_{\text{diff}}$  amplitude with distance.

### 3.2. Influence of realistic 3D velocity structure on the polarizations of $S_{\text{diff}}$ waves

We have shown that  $S_{\text{diff}}$  waves with a significant initial SV component (that is, SV energy that does not result from splitting) cannot be reliably used for shear wave splitting measurements (Section 3.1). Therefore, from here on we will focus our attention on purely SH-polarized  $S_{\text{diff}}$  waves. In particular, we next investigate whether initially SH polarized waves can be influenced by effects other than anisotropy, such that some energy is partitioned into SV on the radial component, potentially mimicking splitting. We first investigate the effects of realistic 3D heterogeneity on  $S_{\text{diff}}$  polarizations. We do so by using the 3D tomography model GyPSuM (Simmons et al., 2010) in the mantle instead of our initial isotropic PREM input model; we retain PREM structure for the crust and the core. We place a source with a focal depth of 0 km at the north pole and the receivers every  $20^\circ$  along a specific longitude. We repeat this every  $20^\circ$  of longitude, starting at the zero meridian, for distances  $103 - 130^\circ$ . These waveforms are shown in Figure 5a for a representative example along longitude  $60^\circ$ . We see that almost no energy arrives on the radial component and the measured splitting intensities are null or very close to it ( $|ST| < 0.3$ ), consistent with a lack of splitting, for all measurements (Figure 5c). Receivers at other longitudes yield similar results. These simulations confirm that we cannot expect a significant redistribution of energy from the transverse to radial components (potentially mimicking splitting) when incorporating a realistic representative 3D tomographic model into our simulations. We repeat this exercise using the 3D tomography model S40RTS (Ritsema et al., 2011), which yields similar results in terms of shear wave polarizations (Figure S3).

We additionally conduct slightly more complicated simulations using the same GyPSuM-based input model and also including a global 20 km thick basal mantle layer of reduced shear velocities, approximating a global ultra-low velocity zone (ULVZ). ULVZs are thin features at the base of the mantle that are characterized by shear wave velocities that are reduced by some tens of per cent compared to the surrounding mantle (e.g., Yu and Garnero, 2018). A global ULVZ has not been observed; this simplified scenario may, however, be a good approximation for zones with widespread ULVZs. We implement S velocity reductions of 30% compared to PREM (decreasing P velocities by 10% and keeping density constant) and conduct simulations for an initially SH polarized  $S_{\text{diff}}$  wave with stations

placed along the zero meridian. Waveforms are shown in Figure 5b as a function of distance and the corresponding splitting intensities are displayed in Figure 5d. We find that  $SI$ -values (representing the amount of radial component energy) are null ( $|SI| < |0.3|$ ) for all distances.

We conclude that, while  $SH_{\text{diff}}$  and  $SV_{\text{diff}}$  waves may indeed accumulate a relative time shift in isotropic structure (Komatitsch et al., 2010; Borgeaud et al., 2016; Parisi et al., 2018), no substantial redistribution of energy from initially SH-polarized  $S_{\text{diff}}$  waves to  $SV_{\text{diff}}$  can be expected in realistic 3D tomographic models or through the influence of ULVZs. In cases for which a slight energy redistribution happens, the waveforms will be strongly distorted from the pulse shape predicted for shear wave splitting and, in practice, would not be mistaken for true splitting.

### 3.3. Polarization anomalies caused by Earth's Coriolis effect

We next evaluate the influence of Earth's Coriolis effect on  $S_{\text{diff}}$  waveforms using SPECFEM3D\_GLOBE. The Earth's Coriolis effect influences all seismic wave propagation, but it has the most noticeable effect on normal modes (Backus and Gilbert, 1961; Masters et al., 1983; Dahlen and Tromp, 1998) and surface waves (e.g., Park and Gilbert, 1986; Tromp, 1994; Snieder and Sens-Schönfelder, 2021). Body waves, particularly shear waves, can be modestly affected (Schoenberg and Censor, 1973; Snieder et al., 2016). As a shear wave propagates through a rotating body, there is a slow rotation of the polarization of shear waves; in contrast, the orientation of wavefronts is not affected by Earth's rotation. The exact change in the polarization of a shear wave will depend on travel time duration, event location, and the raypath relative to Earth's rotation axis, as outlined by Snieder et al. (2016). Here, we determine the deviations of  $S_{\text{diff}}$  from its initial polarization due to the Coriolis effect by comparing two simulations with the same event-receiver setup, for which one simulation excludes and the other includes Earth's rotation (Figure 6).

We find that  $S_{\text{diff}}$  polarization anomalies follow the expected pattern of polarization change due to the Coriolis effect, in which a shear wave's polarization follows a negative cosine curve (Snieder et al., 2016; Creasy et al., in review).  $S_{\text{diff}}$  waves propagating along Earth's rotation axis (north-south) from the event show waveform changes, mainly on the radial component (Figure 6c).  $S_{\text{diff}}$  waves propagating nearly east-west (that is, perpendicular to Earth's rotation axis) produce waveforms for both simulations (rotating and non-rotating) that are completely identical (Figure 6d). Overall, the differences in waveform shapes between the two simulations for the north-south path is small (the amplitudes of the radial component must be doubled to visualize the effect; Figure 6). The polarization change due to Earth's rotation is only  $1 - 3^\circ$  for  $S_{\text{diff}}$  waves, which is generally insignificant considering that error estimates on fast polarization directions are usually at least

$\pm(10 - 15^\circ)$  for splitting measurements (e.g., Long and Silver, 2009). Furthermore, the pattern of polarization anomalies can be easily predicted using a raytracing approach and the effect of Coriolis-induced polarization anomalies can be corrected. Other waves such as direct S are more strongly affected by Earth’s rotation, with polarization anomalies up to almost  $7^\circ$  (Creasy et al., in review).

#### 4. Anisotropic effects on $\text{SH}_{\text{diff}}$ waveforms

##### 4.1. Influence of lowermost mantle anisotropy on $S_{\text{diff}}$ amplitudes

We now focus on the influence that lowermost mantle anisotropy has on  $\text{SH}_{\text{diff}}$  and  $\text{SV}_{\text{diff}}$  amplitudes for initially SH-polarized  $S_{\text{diff}}$  waves. To do so, we run simulations for a model that replaces the bottom 150 km of the mantle of our initial isotropic PREM input model with Ppv anisotropy, as described in Section 2.1, initially using a global layer of anisotropy. The raypath of  $S_{\text{diff}}$  along the CMB can be very long; therefore, we also investigate how the anisotropic signature is influenced by laterally heterogeneous seismic anisotropy, by running models with finite anisotropic regions.

We perform simulations for three different cases. First, we incorporate a global layer of Ppv anisotropy at the base of the mantle (first row in Figure 7); then, we incorporate Ppv anisotropy in the lowermost mantle up to a distance of  $65^\circ$  from the source (second row); third, we incorporate Ppv anisotropy for epicentral distances greater than  $65^\circ$  from the source (third row). For the first case (Figure 7, first row), for which the anisotropic layer is global,  $\text{SH}_{\text{diff}}$  is clearly split, with  $\text{SV}_{\text{diff}}$  energy for the whole distance range. We also observe that for this first case,  $\text{SH}_{\text{diff}}$  and  $\text{SV}_{\text{diff}}$  amplitudes decrease similarly as a function of distance, meaning that the relative amount of energy split to  $\text{SV}_{\text{diff}}$  will reflect the lowermost mantle anisotropy, independent of the size of the anisotropic region. In the second case (Figure 7, second row), we observe splitting (with some energy partitioned to  $\text{SV}_{\text{diff}}$ ) at closer distances ( $< 115^\circ$ ), because lowermost mantle anisotropy is only being sampled at the beginning of the raypath along the CMB.  $\text{SV}_{\text{diff}}$  energy then decreases quickly as a function of distance and has largely died off at an epicentral distance of  $130^\circ$ , relative to  $\text{SH}_{\text{diff}}$ . For the third scenario (Figure 7, third row), at close distances  $S_{\text{diff}}$  waves do not sample seismic anisotropy along the CMB but do sample anisotropy after they leave the CMB on their (long) path through the  $D''$  layer. At slightly larger distances ( $\sim 115^\circ$ ), they start sampling the anisotropy along the CMB, leading to significant splitting.

These results have some important implications regarding  $\text{SH}_{\text{diff}}$  splitting measurements performed on real data. In the absence of upper mantle anisotropy, our simulations demonstrate the following:

- Seismic anisotropy in the lowermost mantle generally leads to splitting of energy from SH to SV for initially SH-polarized  $S_{\text{diff}}$  waves. (For the real Earth, recognizing splitting in record sections will not be as straightforward as in Figure 7 because  $SV_{\text{diff}}$  energy may not have originated from splitting, but may instead be due to the initial source polarization, as discussed in Section 3).
- Relatedly, if waveforms similar to those predicted for cases one and two (Figure 7; with  $D''$  anisotropy sampled in the beginning of the raypath, or along the whole raypath) were observed in real data, radial energy could not directly be attributed to splitting due to lowermost mantle anisotropy without considering the source mechanism. The possibility of  $SV_{\text{diff}}$  energy due to effects other than anisotropy can only be excluded if the focal mechanism, and therefore the amount of initial SV energy, is known.
- Assuming that it can be shown (via knowledge of the focal mechanism and/or wavefield simulations) that observations of significant SV energy would not be expected in the absence of lowermost mantle anisotropy, deep mantle anisotropy must be present.  $S_{\text{diff}}$  splitting serves as a straightforward diagnostic of lowermost mantle anisotropy in this case. However, it will likely be challenging to infer exactly where along the raypath lowermost mantle anisotropy is present or what the lateral extent of the anisotropic region is.
- Only for the case shown in the third row of Figure 7, for which  $S_{\text{diff}}$  waves are not sampling  $D''$  anisotropy at close distances, and therefore there is an increase in  $SV_{\text{diff}}$  amplitudes as a function of distance, can lowermost mantle anisotropy be diagnosed without knowledge of the focal mechanism. An increase of radial amplitudes as a function of distance while transverse amplitudes are decreasing (without any enigmatic waveform effects) almost certainly reflects the presence of lowermost mantle anisotropy (see waveform behavior in Section 3). Additionally, for this case, it should also be possible to localize the anisotropy by identifying which  $S_{\text{diff}}$  raypaths are associated with an increase of  $SV_{\text{diff}}$  amplitudes as a function of distance.

In addition to isotropic PREM, we also incorporate the 3D tomography model GyPSuM in the mantle (replacing PREM at those depths) and repeat the simulations described above, incorporating lowermost mantle anisotropy. The results are shown in Supplementary Figure S4. Apart from the arrival times of the  $S_{\text{diff}}$  waves and some minor effects to the waveforms, the general amplitude trends are the same as in as in Figure 7, so our conclusions do not depend on the details of long-wavelength mantle heterogeneity.

#### 4.2. Influence of source-side anisotropy on $SH_{\text{diff}}$ splitting estimates

We have already shown that, if there is a non-negligible initial  $SV_{\text{diff}}$  component,  $SV_{\text{diff}}$  energy could potentially mimic splitting, even if no anisotropy is present. However, even if the focal mechanism is known and it can be shown that  $S_{\text{diff}}$  should be (almost) fully SH polarized,  $S_{\text{diff}}$  may sample seismic anisotropy in the upper- or mid-mantle on the source side, leading to more SV energy than would be expected for the isotropic case. Here, we investigate how anisotropy near the seismic source can affect estimates of splitting due to lowermost mantle anisotropy.

We first incorporate a 200 km thick anisotropic layer in the upper mantle just beneath the source, with no anisotropy in the lowermost mantle, and investigate the cases of moderate (2% anisotropic strength) and relatively strong (4%) upper mantle source-side anisotropy. For the case of strong HTI upper mantle anisotropy on the source side (and no anisotropy on the receiver side), direct S waves accumulate a time delay of  $\sim 1.8$  s for an epicentral distance of  $60^\circ$ , which we determined by running synthetic simulations and measuring the resulting shear wave splitting. The time delay is about half as large for the moderate splitting case. (In general, we would expect splitting of  $S_{\text{diff}}$  waves to be weaker than for S, because SV energy will be lost to the core upon diffraction of these waves.) In order to characterize and quantify splitting of  $S_{\text{diff}}$  waves due to source-side anisotropy, we calculate synthetic seismograms using AxiSEM3D for the range of (isotropic) lowermost mantle properties that were investigated in Section 3.1, and also incorporate the GyPSuM tomography model for the mantle into our simulations. Then, we measure the splitting intensity due to source-side anisotropy using SplitRacer.

Figure 8 shows the synthetic splitting intensities as a function of epicentral distance for a moderate strength of upper mantle source-side anisotropy (200 km thick layer, 2% HTI). We see that, largely independent of lowermost mantle properties, the contribution of source-side anisotropy to  $S_{\text{diff}}$  splitting is quite modest and would thus unlikely be misdiagnosed as strong lowermost mantle splitting (Figure 7). We do see absolute  $SI$ -values that are in some cases (slightly) larger than 0.3 for distances that are smaller than  $115^\circ$ ; in particular, for the GyPSuM and the linear gradient scenario with a lowermost mantle velocity of  $7.5 \frac{\text{km}}{\text{s}}$ , the absolute  $SI$ -values exceed 0.3 in a few cases. In general, however, moderate source-side anisotropy would not be enough to produce significant splitting in  $S_{\text{diff}}$  seismograms. Therefore, it is not likely to be mistaken for lowermost mantle anisotropy.

For the strong source-side anisotropy case, the results are more complicated, as shown in Supplementary Figure S5: For the case of low  $Q_\mu$  ( $= 75$ ) and for lowermost mantle velocities that are lower than PREM ( $-2\%$ ), the splitting contribution from the source side can propagate through to the receiver and potentially be mistaken for lowermost mantle

splitting; for all other investigated scenarios, absolute source-side splitting intensities are mostly lower than 0.3. Another general observation is that the influence of source-side anisotropy tends to decrease with increasing distance (because  $SV_{\text{diff}}$  dies off faster than  $SH_{\text{diff}}$ ). Despite this, however, our results indicate that for regions with strong source-side anisotropy,  $S_{\text{diff}}$  waves should be corrected for this contribution to reliably measure lowermost mantle splitting. The source-side contribution can, for example, be investigated using other waves such as direct S (e.g., Russo et al., 2010; Foley and Long, 2011; Mohiuddin et al., 2015).

Our observation that strong source-side anisotropy can cause  $S_{\text{diff}}$  splitting if lowermost mantle velocities are lower than PREM (Figure 8b) poses the question of whether ULVZs can potentially have an even larger effect. In order to investigate their effects, we incorporate a global 20 km thick layer of reduced velocities into our input model. Because we expect results to depend on how much the shear-wave velocity is reduced, we conduct multiple simulations for different S wave velocity reductions. Because the results are generally very similar for different shear velocity reductions, we show the two endmembers with 2% and 20% velocity reduction in Figure 9. (We reduce P velocities by 1/3 of the value for S velocities and keep density unchanged.) Trade-offs between velocity reduction and thickness of the anisotropic layer likely exist, but are not explicitly explored here. We find that only a couple of measurements at small distances are (slightly) split, while all other measurements are null, indicating that source-side upper mantle anisotropy would not generally be mistaken for a lowermost mantle contribution if thin low velocity anomalies are present at the CMB. We conducted similar simulations for different velocity reduction percentages, which confirm this impression (Figure S6).

#### 4.3. Influence of lowermost mantle anisotropy on $SH_{\text{diff}}$ splitting measurements

We have shown in Section 4.1 how  $SV$  amplitudes behave as a function of distance in the presence of lowermost mantle anisotropy. Further, we have shown that strong source-side anisotropy can potentially cause  $S_{\text{diff}}$  splitting and can thus potentially be mistaken for a lowermost mantle anisotropy contribution in some cases if not properly accounted for (Section 4.2). Here, we go one step further and explicitly measure shear wave splitting (via the splitting intensity) for scenarios that include lowermost mantle anisotropy. We also investigate whether and how the presence of source-side anisotropy affects estimates of splitting parameters due to lowermost mantle anisotropy.

For this purpose, we compute synthetic seismograms for multiple scenarios. As in Section 4.1, we investigate how splitting measurements on initially SH-polarized  $S_{\text{diff}}$  waves are influenced by anisotropy located at different regions along the raypath. We incorporate Ppv lowermost mantle anisotropy in the mantle either for a global anisotropic layer in the

lowermost mantle, for epicentral distances larger than  $65^\circ$  (measured from the source), or less than  $65^\circ$ . In order to achieve realistic splitting intensity values for these models, the anisotropic strength of the Ppv elastic tensor for the deep mantle is reduced, as described in Section 2.1. We use two different background models for these synthetics: a) isotropic PREM or b) isotropic PREM, but with the mantle structure replaced by the GyPSuM tomography model. For each of these cases, we investigate how the addition of upper mantle anisotropy influences the shear wave splitting measurements.

We show results for moderately strong HTI anisotropy in the upper mantle in Figure 10. We observe that splitting intensities are relatively constant as a function of distance for a full global anisotropic layer, while they either increase or decrease with epicentral distance for the two other cases. The incorporation of (isotropic) 3D heterogeneity via the GyPSuM tomography model has only a slight influence on the measured splitting intensities compared to isotropic PREM. Also, we find that moderate source-side anisotropy does not strongly affect the measured splitting. This is generally also true for strong source-side anisotropy (Supplementary Figure S7), although the strong upper mantle anisotropy has a slightly larger influence, as expected (see Section 4.2). Compared to a moderate upper mantle anisotropy strength, the 95% confidence intervals of the splitting measurements tend to become larger for strong upper mantle anisotropy.

From the simulations that include lowermost mantle anisotropy, we infer that even strong source-side anisotropy likely only has minor effects on the measured overall splitting if the lowermost mantle anisotropy is sufficiently strong. Because it is difficult to ensure that this condition is met, however, we nevertheless recommend only using data that does not sample strong anisotropy in the source side upper mantle, which can be assured using data from phases other than  $S_{\text{diff}}$ . Moreover, we have demonstrated that including realistic 3D heterogeneity does not have a large effect on the measured  $S_{\text{diff}}$  splitting parameters.

## 5. Discussion

### 5.1. Strategy for $S_{\text{diff}}$ splitting measurements

We have argued that in order to avoid introducing large uncertainties, splitting should only be measured on  $S_{\text{diff}}$  waves that have a negligible initial  $SV_{\text{diff}}$  component. We have shown in Section 3.1 that the assumption that  $SV_{\text{diff}}$  has died off at any particular distance, and therefore that all SV energy is due to splitting, cannot be made universally. However, there are some examples for which this assumption is indeed appropriate. Specifically, when  $S_{\text{diff}}$  waves sample regions in which the lowermost mantle velocity is greater than average and for certain attenuation structures,  $SV_{\text{diff}}$  waves are predicted to die off quickly compared to  $SH_{\text{diff}}$ . There is, however, substantial uncertainty regarding lowermost mantle

properties, which makes it difficult to ensure that these conditions are met for any source-receiver pair. If isotropic lowermost mantle conditions and  $S_{\text{diff}}$  initial polarization are known perfectly, seismic anisotropy could be characterized if  $S_{\text{diff}}$  has a mixed  $SH_{\text{diff}}$  versus  $SV_{\text{diff}}$  initial polarization, for example through a waveform modeling approach. However, in practice, there is significant uncertainty about the detailed properties of the lowermost mantle. Therefore, we suggest to ensure that  $S_{\text{diff}}$  is primarily SH polarized via knowledge of the focal mechanism. Before measuring  $S_{\text{diff}}$  splitting, it should be verified that for the selected source-receiver configuration, little or no  $SV_{\text{diff}}$  energy can be expected to arrive at the receiver in an isotropic Earth. This evaluation can be done by using full-wave simulations (by incorporating the known moment tensor), as we do here, or by calculating the initial polarization based on the moment tensor. These simulations can and should consider a priori information about the velocity and attenuation structure of the particular region. It may not be sufficient to rely on isotropic PREM to investigate whether negligible  $SV_{\text{diff}}$  energy can be expected, particularly if raypaths sample structures such as LLVPs or regions with higher than average velocities.

We have also shown in Section 4 that, even for cases in which  $S_{\text{diff}}$  would be primarily SH polarized in an isotropic Earth, splitting can occur in the upper mantle on the source side, which can potentially be misinterpreted as evidence of lowermost mantle anisotropy if one does not account for this possibility. Events associated with regions of strong source-side anisotropy can be avoided by explicitly measuring source-side splitting using direct S or by focusing on particularly deep events (i.e.,  $> 400$  km). While the uppermost lower mantle and the transition zone have been shown to be anisotropic in some cases, particularly in subduction zone settings, they generally produce splitting with delay times  $< 1$  s (e.g., Foley and Long, 2011; Lynner and Long, 2015; Mohiuddin et al., 2015). This means that deep events ( $> 400$  km) can generally be used for  $S_{\text{diff}}$  splitting measurements because only relatively weak source-side splitting ( $\delta t < 1$  s) can be expected for them. In any case, it must be ensured in  $S_{\text{diff}}$  splitting analyses that candidate  $SH_{\text{diff}}$  waves sample only weak to moderate source-side anisotropy.

Apart from potentially sampling source-side and lowermost mantle anisotropy,  $S_{\text{diff}}$  waves will generally also be affected by anisotropy in the receiver-side upper mantle (and perhaps the crust), just like other waves used to study the deep mantle. A feasible approach to characterize upper mantle anisotropy beneath stations is to measure SKS splitting over a range of backazimuths, as SKS waves generally reflect contributions from the upper mantle beneath the receiver in most cases (e.g., Becker et al., 2015).  $S_{\text{diff}}$  waves can then be explicitly corrected for this contribution before measuring  $D''$ -associated splitting. Such an approach has been shown to accurately retrieve the fast polarization direction,  $\phi$ , for direct

source side S splitting; uncertainties of  $\delta t$  measurements are large, however (Wolf et al., 2022a). While explicit receiver side corrections are the most straightforward way to account for upper mantle anisotropy beneath the receiver, there may also be alternative strategies, particularly in cases where array data are available. (We will discuss alternatives in Section 5.3.) In any case, it should be demonstrated that any measured  $S_{\text{diff}}$  splitting signature cannot be explained by receiver side upper mantle anisotropy, and explicit receiver side corrections are often appropriate. In some cases, it may only be possible to demonstrate that  $S_{\text{diff}}$  is affected by lowermost mantle anisotropy, without the ability to explicitly measure the lowermost mantle associated splitting parameters (due to uncertainties associated with receiver-side corrections).

After measuring the lowermost mantle-associated splitting parameters, it should be considered that there is significant uncertainty regarding where along the  $S_{\text{diff}}$  raypath splitting has occurred. In general, anisotropy sampled earlier along the  $D''$  portion of the ray's path will affect the measured splitting parameters at the station less than anisotropy that is sampled later on the raypath (Section 4.1), due to full-wave effects. A single measurement, however, does not suffice to show where exactly seismic anisotropy is present in the lowermost mantle. Inferences on the likely distribution of anisotropy may be possible when multiple measurements from dense seismic arrays are interpreted together; furthermore, anisotropy may be localized by taking advantage of crossing raypaths (e.g., Nowacki et al., 2010; Ford et al., 2015; Creasy et al., 2021). We also point out that the measured splitting at the receiver will be affected by a large  $D''$  volume, as the sensitivity kernels for  $S_{\text{diff}}$  waves at the base of the mantle are broad.

To summarize, our suggested workflow for  $S_{\text{diff}}$  splitting measurements to detect lowermost mantle anisotropy includes the following steps:

1. Ensure that  $S_{\text{diff}}$  can be expected to be almost fully  $SH_{\text{diff}}$  polarized in an isotropic Earth for the raypaths under study. This can, for example, be done via full-wave simulations.
2. Exclude a substantial source-side upper mantle contribution, either by characterizing the source-side anisotropy through other phases (e.g., direct S) or by focusing on deep earthquakes ( $> 400$  km).
3. Measure  $S_{\text{diff}}$  splitting parameters using standard techniques.
4. If necessary, explicitly correct for receiver side upper mantle anisotropy.
5. Interpret  $S_{\text{diff}}$  splitting measurements in terms of lowermost mantle anisotropy, considering that it is often unclear where exactly along the raypath lowermost mantle anisotropy was sampled.

### 5.2. $S_{\text{diff}}$ splitting strategy in light of previous work

Previous work investigated apparent time delays between  $\text{SH}_{\text{diff}}$  and  $\text{SV}_{\text{diff}}$  for simple Earth models (Komatitsch et al., 2010), different mantle attenuation structure (Borgeaud et al., 2016), and realistic 3D velocity structure (Parisi et al., 2018). In these studies, events were chosen such that  $S_{\text{diff}}$  waves are partially SH and partially SV polarized, with both components generally having a similar amplitude. The radial energy that produced differential  $\text{SH}_{\text{diff}}\text{-SV}_{\text{diff}}$  travel times in absence of seismic anisotropy in previous studies (Komatitsch et al., 2010; Borgeaud et al., 2016; Parisi et al., 2018) was mostly due to initial SV energy propagating along the CMB. In practice, however,  $S_{\text{diff}}$  phases are often primarily SH polarized. We have suggested in this study that  $S_{\text{diff}}$  waves can be used for splitting measurements for cases in which  $\text{SH}_{\text{diff}}$  can be expected to be much larger than  $\text{SV}_{\text{diff}}$ , thereby excluding effects similar to those reported in previous papers. Additionally, instead of focusing on differential  $\text{SH}_{\text{diff}}\text{-SV}_{\text{diff}}$  travel times which often result from waveform distortions, we have explicitly measured splitting parameters ( $\phi$ ,  $\delta t$ ;  $SI$ ) in our study. This approach helps avoid the misinterpretation of  $\text{SV}_{\text{diff}}$  energy that results from isotropic structure (for example, due to the presence of ULVZs or phase interference) as splitting. The reason for this is that well-constrained splitting parameters will only be obtained (for an initially SH-polarized  $S_{\text{diff}}$  phase) if the radial component has a similar shape as the transverse component time derivative. To summarize, previous studies have analyzed differential  $\text{SH}_{\text{diff}}\text{-SV}_{\text{diff}}$  travel times from partially SH and SV-polarized  $S_{\text{diff}}$  waves. We measure splitting parameters for  $S_{\text{diff}}$  waves that can be assumed to initially be SH-polarized, a different approach than that taken in this work. The results from this study, including our suggested splitting strategy, are fully consistent with the previous findings of Komatitsch et al. (2010), Borgeaud et al. (2016) and Parisi et al. (2018).

### 5.3. Real data example

In order to illustrate our suggested  $S_{\text{diff}}$  splitting strategy, we present a real data example using EarthScope USArray data from North America. We focus on a source-receiver geometry for which  $S_{\text{diff}}$  splitting has been identified previously (Wolf and Long, 2022) but expand our analysis to consider additional earthquakes. We use three events that occurred in 2009 and 2010 beneath the Celebes Sea; at this time, a large number of USArray Transportable Array stations were deployed at an epicentral distance range of  $101^\circ$  to  $120^\circ$ . Figure 11a illustrates our source-receiver geometry sampling the lowermost mantle beneath the northern Pacific Ocean, where we highlight the sections of the raypath along the CMB. The station selection for all three events is very similar (but not identical, because we discard low-quality data from some stations and because the events occurred at different times). The substantial overlap also means that the raypaths are similar for all three events.

*Step 1: Initial polarization of  $S_{\text{diff}}$*

As a first step, following the strategy laid out in Section 5.1, we investigate the expected  $S_{\text{diff}}$  polarizations for each event. We obtain the focal mechanisms of all three events from the USGS database and conduct synthetic simulations using AxiSEM3D (for the same source-receiver configurations as for the real data). The background velocity model that we use is isotropic PREM, but we replace the velocities in the lowermost mantle with velocities from a (isotropic) local 3-D shear wave velocity model beneath the northern Pacific Ocean (Suzuki et al., 2021) to approximate the local velocity structure. We incorporate the Suzuki et al. (2021) model rather than a global model here because it represents smaller scale velocity heterogeneity in the lowermost mantle of our study region. We do not incorporate ULVZs because we have shown before that SV energy due to ULVZs is unlikely to mimic splitting (Section 3.2), and because no ULVZs have been unambiguously identified in our region of interest (Yu and Garnero, 2018). The synthetic radial and transverse component seismograms for three simulations are shown in Figure 11c-e. Fortunately, for all three events, little or no  $SV_{\text{diff}}$  energy would be expected in an isotropic Earth, although predicted  $SV_{\text{diff}}$  amplitudes for event 2009-10-07 are slightly larger than for the other two events. Despite that, these modeling results indicate that  $S_{\text{diff}}$  splitting analyses can be conducted for all three events, as any significant SV energy can be attributed to splitting behavior and not isotropic structure.

*Step 2: Influence of source-side anisotropy*

Second, we investigate the possibility of source-side anisotropy contributions to our waveforms. All the three events used in this study occurred at depths greater than 580 km. As argued in Section 4.3 and Section 5.1, significant source-side anisotropy (with delay times  $> 1$  s) is unlikely for such deep events (e.g., Foley and Long, 2011; Lynner and Long, 2015). This was also explicitly shown by Mohiuddin et al. (2015) for the Celebes Sea, where the three earthquakes under study occurred.

*Step 3:  $S_{\text{diff}}$  splitting due to lowermost mantle anisotropy*

Next, we investigate whether the  $S_{\text{diff}}$  waves from our three events show any evidence of lowermost mantle anisotropy. We focus on a subset of the data that shows convincing evidence for  $SV_{\text{diff}}$  energy due to  $D''$ -associated splitting at azimuths  $> 43^\circ$  and distances  $> 110^\circ$  for all three events (Figure 12), building upon work from Wolf and Long (2022). In Wolf and Long (2022), a similar subset of  $S_{\text{diff}}$  data for event 2010-10-07 was analyzed, in combination with measurements of differential SKS-SKKS splitting. In that previous work, we mainly based our interpretation in that work on SKS-SKKS differential splitting results. With the results presented in this paper, we can now be fully confident that the

observed  $SV_{\text{diff}}$  energy indeed reflects splitting due to deep mantle anisotropy. Here, we extend our analysis to two additional events and measure  $S_{\text{diff}}$  splitting due to lowermost mantle anisotropy for all three earthquakes.

*Step 4: Receiver-side anisotropy contribution*

Figure 12 shows  $S_{\text{diff}}$  waveforms for all three events aligned via cross-correlation of the transverse components. Energy is clearly split to the radial component for all events; in fact, the stacked waveforms (black lines; Figure 12) look very similar for all three earthquakes. Figure 13a-c is similar to Figure 12 (for the same source-receiver pairs) but for SKS waves. Figure 13 demonstrates that the splitting of energy from the transverse to the radial component of  $S_{\text{diff}}$  for these events cannot be explained by the presence of upper mantle anisotropy beneath the receiver only. This conclusion can be made because no strong, coherent splitting of energy from the radial to the transverse components can be observed for SKS, suggesting that the upper mantle anisotropy beneath the receivers generally causes relatively weak and incoherent splitting for this event. This in turn implies that differences in splitting between  $S_{\text{diff}}$  and SKS originate from contributions to  $S_{\text{diff}}$  splitting from anisotropy along the portion of the raypath through the lowermost mantle. This result is not entirely surprising, considering that the upper mantle splitting pattern from the IRIS splitting database (IRIS DMC, 2012) shows relatively weak and variable splitting across the array (Figure 13d). We infer from this exercise that for the  $S_{\text{diff}}$  waves (measured and stacked across the same set of stations as SKS) the receiver side upper mantle contribution can be expected to largely average out as well.

We next quantitatively investigate the degree to which the waveforms are influenced by lowermost vs. upper mantle anisotropy by measuring SKS and  $S_{\text{diff}}$  splitting intensities for all individual seismograms from our three events (recorded at the stations shown in Figure 11). We compare these two phases because differences between SKS and  $S_{\text{diff}}$  splitting likely reflect a contribution from  $D''$ , as argued above. Furthermore, we have previously shown that for this source-receiver geometry, SKS is likely primarily influenced by receiver side upper mantle anisotropy (Wolf and Long, 2022).

Our measurements of SKS and  $S_{\text{diff}}$  splitting intensities for individual seismograms are shown in Figure 14 as a function of epicentral distance from the source. We find that while SKS splitting intensities tend to decrease as a function of distance and scatter around zero for distances that are larger than  $110^\circ$ ,  $S_{\text{diff}}$  waves for all three events, in contrast, consistently show a pronounced increase in splitting intensities at an epicentral distance of approximately  $110^\circ$ . This increase occurs at slightly larger distances for event 2009-10-07; this event occurred slightly farther away from the USArray stations than the other two events (Figure 11a).  $S_{\text{diff}}$  splitting intensities plateau for distances  $> 110^\circ$  (Figure 14). Thus,

the anisotropic signature apparently does not change as a function of distance, indicating that  $S_{\text{diff}}$  is likely sampling a large, uniformly anisotropic region at the base of the mantle. This is also supported by the observation of coherent and uniform  $S_{\text{diff}}$  splitting in the record sections that show the waveforms for these distances (Figure 12). The observation that SKS splitting intensities scatter around zero for distances from  $110^\circ$  to  $120^\circ$  indicates the presence of generally fairly weak upper mantle anisotropy that varies laterally across the area in which the receivers are positioned. This is consistent with previously published estimates of SKS splitting at these stations (Figure 13d). In contrast to SKS splitting,  $S_{\text{diff}}$  splitting is consistently very strong at epicentral distances larger than  $110^\circ$ , showing a distinctly different pattern than SKS. This indicates a considerable influence of lowermost mantle anisotropy on  $S_{\text{diff}}$  waves.

We emphasize that the approach we have taken here, which relies on visual inspection of record sections and measurements of splitting intensity as a function of distance, can only be used if  $S_{\text{diff}}$  waves from one event are recorded across a large seismic array. Without such a favorable source-receiver configuration, patterns of splitting intensity with distance could not be resolved well; furthermore, if  $S_{\text{diff}}$  waves are too noisy or stations are too sparse, it may not be possible to reliably resolve trends of the splitting intensity. Additionally, this particular dataset allows us to measure splitting from single station  $S_{\text{diff}}$  data without explicitly correcting for the upper mantle contribution, as discussed below; for other datasets, explicit receiver-side upper mantle corrections will generally be needed.

*Step 5: Interpretation of  $S_{\text{diff}}$  splitting parameters in terms of deep mantle anisotropy*

Our next step is to measure the lowermost mantle associated splitting parameters. To do this, we again focus on the subset of stations for which Wolf and Long (2022) demonstrated a strong lowermost mantle anisotropy contribution for event 2009-10-07. Specifically, we focus on the distances  $> 110^\circ$  and azimuths  $< 43^\circ$  and take an approach that involves stacking our data. We note that data should only be stacked over a distance and azimuth range for which a uniform lowermost mantle signature can be inferred based on the waveform behavior. In our case, the waveforms in Figure 12 indicate that splitting is uniform. Additionally, we measure  $S_{\text{diff}}$  splitting parameters of the single station  $S_{\text{diff}}$  seismograms, which yields similar  $(\phi', \delta t)$  measurements over the whole distance/azimuth range of interest (Figures S8-S10), indicating that the influence of lowermost anisotropy is more dominant than the (weak) upper mantle receiver side anisotropy (Figure 13d).

We now focus on the  $S_{\text{diff}}$  waveforms for the epicentral distance ( $> 110^\circ$ ) and azimuth ( $< 43^\circ$ ) ranges for which a lowermost mantle contribution to splitting has been observed (and for which the corresponding SKS stack splitting is null). We align the  $S_{\text{diff}}$  waveforms by cross-correlation of the transverse components as shown in Figure 15a-b. For all three

events, we observe a strong and coherent splitting signal, expressed in  $S_{\text{diff}}$  amplitudes, caused by the contribution of lowermost mantle anisotropy. In order to increase SNR and thus confidence in our measurements, in addition to measuring splitting intensities for individual seismograms (Figure 11), we also stack the  $S_{\text{diff}}$  waveforms across the array and measure splitting parameters ( $\phi$ ,  $\delta t$ ) from these  $S_{\text{diff}}$  stacks. Results for one event are shown in Figure 15, which shows the splitting diagnostic plots for event 2010-10-04. We do not implement an explicit correction for the effect of the Coriolis force because we have shown that these effects are generally negligible (Section 3.3). We find that the splitting parameters measured for each of the three events agree extremely well (see Supplementary Figures S11 and S12 for events 2010-10-07 and 2010-07-29), with a maximum difference of  $3^\circ$  for  $\phi$  and 0.1 s for  $\delta t$  (the average values are  $\phi \approx 134^\circ$  and  $\delta t \approx 1.5$  s). The splitting measurements from the stacks agree with the single station splitting measurements for this dataset (Supplementary Figures S8-S10) but are more robust.

As a final step,  $S_{\text{diff}}$  splitting measurements can be interpreted in terms of lowermost mantle deformation and flow directions. This is best accomplished via a forward modeling approach; in particular, we can carry out global wavefield simulations for different lowermost mantle anisotropy scenarios and compare predictions to data. We have previously applied such an approach for event 2010-10-07 in our dataset, which was modeled simultaneously with observations of  $D''$ -associated splitting of SKKS waves (Wolf and Long, 2022). Our previous study showed that  $S_{\text{diff}}$  splitting for the source-receiver pairs examined in this study can be explained with a model that invokes lattice-preferred orientation of Ppv resulting from slab-driven flow in the lowermost mantle beneath the northeastern Pacific Ocean. Although we used only one event from that study to conduct  $S_{\text{diff}}$  splitting measurements, the results from all three events examined here are highly consistent with the results from Wolf and Long (2022). Thus, the three measurements can also be explained by the same deformation scenario.

#### 5.4. $S_{\text{diff}}$ splitting analyses on single-station data: Limitations and ways forward

One main advantage with the array data used in Section 5.3 is that the upper mantle splitting contribution is such that explicit anisotropy corrections for the upper mantle on the receiver side are not needed. In many or most cases, however, explicit corrections for upper mantle anisotropy may need to be applied. Even in such cases, however, it may be useful to stack data to improve signal-to-noise ratios. Apart from the approach used here, there are various other strategies to account for the influence of receiver side anisotropy on  $S_{\text{diff}}$  waves. A common approach is to measure SKS splitting for every station, preferably using multiple events from different backazimuths (e.g., Lynner and Long, 2014; Lynner and Long, 2015).  $S_{\text{diff}}$  waveforms can then be corrected for the upper mantle associated splitting

parameters obtained this way. We would advise against measuring SKS splitting for a few backazimuths only because splitting beneath any particular station may be complex, and any single SKS splitting measurement may potentially be influenced by lowermost mantle anisotropy (e.g., Wolf et al., 2022a). Alternatively, a strategy to account for the  $S_{\text{diff}}$  upper mantle contribution can be to correct  $S_{\text{diff}}$  for the SKS/SKKS splitting parameters for the same source receiver configuration, if SKS and SKKS are split similarly. (If they are not, at least one of the phases is likely influenced by lowermost mantle anisotropy and both measurements cannot be assumed to be due to upper mantle anisotropy only.) A major disadvantage of this strategy is that well-constrained SKS, SKKS and  $S_{\text{diff}}$  splitting parameters would be required for the same source-receiver configuration. Finding data for which it is possible to obtain such good splitting measurements from three phases in one seismogram may be challenging. A special case of this approach is if SKS and SKKS splitting are null for the raypath under study. In this case,  $S_{\text{diff}}$  splitting could be interpreted to be due to lowermost mantle anisotropy, and no corrections would need to be applied.

The investigation of  $S_{\text{diff}}$  waves recorded across a dense, large-aperture array makes patterns of splitting more obvious than they would be for single station measurements (for example, the opposite trends of SKS and  $S_{\text{diff}}$  splitting intensities that is shown in Figure 14). Applying our observational strategy to an  $S_{\text{diff}}$  dataset from a relatively large array is also helpful in localizing the anisotropy. In our case, for example, we know that the  $S_{\text{diff}}$  waves show a particularly strong signature of lowermost mantle anisotropy for distances  $> 110^\circ$ . With this knowledge, the dimensions of the anisotropic region in the lowermost mantle can be (partially) inferred. In contrast, for a single  $S_{\text{diff}}$  splitting measurement it would not be possible to infer where the anisotropy is localized along the  $S_{\text{diff}}$  raypath. Some caution is also warranted when stacking waveforms across a large array (and thus averaging anisotropy across a relatively large portion of the lowermost mantle). For our dataset this approach is justified, because splitting is coherent for the  $S_{\text{diff}}$  waves sampling the  $D''$  region under study (Figure 11a and Supplementary Figures S8-S10). In other cases, however, anisotropy could potentially vary laterally, yielding variability in splitting. In general, only those waveforms that show coherent splitting should be stacked, which may mean focusing on smaller distance/azimuth intervals.

## 6. Conclusion

In this work, we have investigated isotropic and anisotropic effects on  $S_{\text{diff}}$  polarizations in order to understand whether and how the splitting of  $S_{\text{diff}}$  waves can be used to infer lowermost mantle anisotropy. We have used full-wave simulations to demonstrate, for a range of isotropic mantle models, that  $SV_{\text{diff}}$  amplitudes do not necessarily decrease substantially

faster as function of distance than  $SH_{\text{diff}}$  amplitudes. Thus, only  $S_{\text{diff}}$  waves with a negligible initial SV component should be used to conduct  $D''$  shear wave splitting measurements, and care must be taken to select suitable events for analysis. In order to evaluate the effects of upper and mid-mantle anisotropy on  $S_{\text{diff}}$  splitting, we tested models with anisotropy near the source and found that weak or moderate source-side splitting ( $\delta t_{\text{source}} < 1$  s) has minimal effects on  $S_{\text{diff}}$  waves in most models. However, strong source-side anisotropy can cause  $S_{\text{diff}}$  splitting and should be avoided in lowermost mantle anisotropy studies. We have further shown that lowermost mantle anisotropy can be recognized by strong splitting of energy from  $SH_{\text{diff}}$  to  $SV_{\text{diff}}$  (for initially SH-polarized  $S_{\text{diff}}$  waves), while realistic isotropic Earth structure does not mimic such a behavior. Our simulations have demonstrated that  $S_{\text{diff}}$  waves can, indeed, be used to infer lowermost mantle anisotropy under many conditions. These insights have helped us formulate a strategy for carrying out measurements of  $S_{\text{diff}}$  splitting due to  $D''$  anisotropy. Important considerations include showing that the  $S_{\text{diff}}$  waves of interest would be almost completely SH polarized in an isotropic Earth and are not influenced by strong source-side anisotropy ( $\delta t_{\text{source}} < 1$  s). To illustrate our proposed splitting strategy, we conducted a systematic  $S_{\text{diff}}$  splitting analysis for real waveforms for western Pacific earthquakes measured at USArray stations, revealing evidence for strong, coherent anisotropy in the lowermost mantle beneath the northeastern Pacific.

### Acknowledgements

This work was funded by Yale University and by the U.S. National Science Foundation via grant EAR-2026917 to MDL, grant EAR-1855206 to NC, and grant EAR-1853911 to EG. We thank the Yale Center for Research Computing for providing the research computing infrastructure for this study. We are also grateful to the Extreme Science and Engineering Discovery Environment (XSEDE) Texas Advanced Computing Center (TACC) at The University of Texas at Austin through allocation TG-EES200011 using XSEDE resources (Towns et al., 2014). We acknowledge the Yale seismology group for helpful discussions. The Generic Mapping Tools (Wessel and Smith, 1998), ObsPy (Beyreuther et al., 2010), MSAT (Walker and Wookey, 2012) and SplitRacer (Reiss and Rmpker, 2017) were used in this research. We are grateful to the editor, Ana Ferreira, and an anonymous reviewer for their constructive comments that helped us improve the manuscript.

### Data availability

The synthetic seismograms for this study were computed using `AxiSEM3D` and `SPECFEM3D_GLOBE`, which are publicly available at <https://github.com/AxiSEMunity> and <https://geodynamics.org>.

org/cig/software/specfem3d\_globe. All USArray data (IRIS Transportable Array, 2003) were downloaded through IRIS (<https://service.iris.edu/>).

ORIGINAL UNEDITED MANUSCRIPT

Figures:

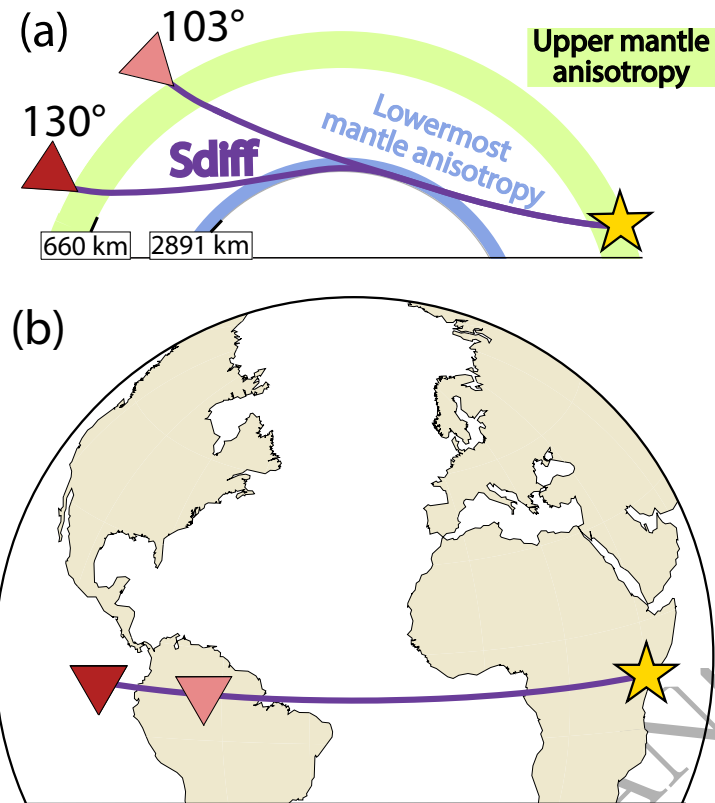


Figure 1: Schematic illustration of a typical source-receiver configuration in our numerical simulations. The  $S_{diff}$  raypath is shown by a solid purple line. (a) Cross-section through Earth. Stations are represented as red triangles and the source as a yellow star.  $S_{diff}$  potentially travels through upper mantle anisotropy at source and receiver side (green), and lowermost mantle anisotropy (blue). (b) Map view of the source, located at the equator (at longitude  $-90^\circ$ ), and the  $S_{diff}$  raypath to stations located in a distance of  $103^\circ$  and  $130^\circ$  at the equator.

ORIGINAL UNEDITED MANUSCRIPT

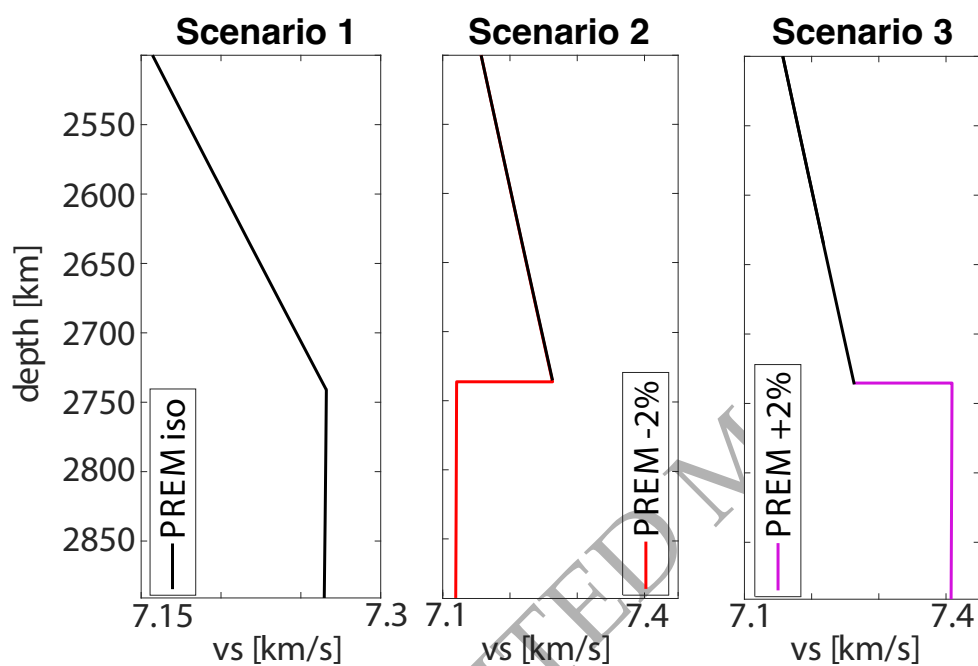


Figure 2: 1D models velocity models used in our simulations. Scenario 1: Isotropic PREM (Dziewonski and Anderson, 1981); scenario 2: Isotropic PREM, with 2% lower velocities in the lowermost 150 km of the mantle; scenario 3: Isotropic PREM, with 2% increased velocities in the lowermost 150 km of the mantle.

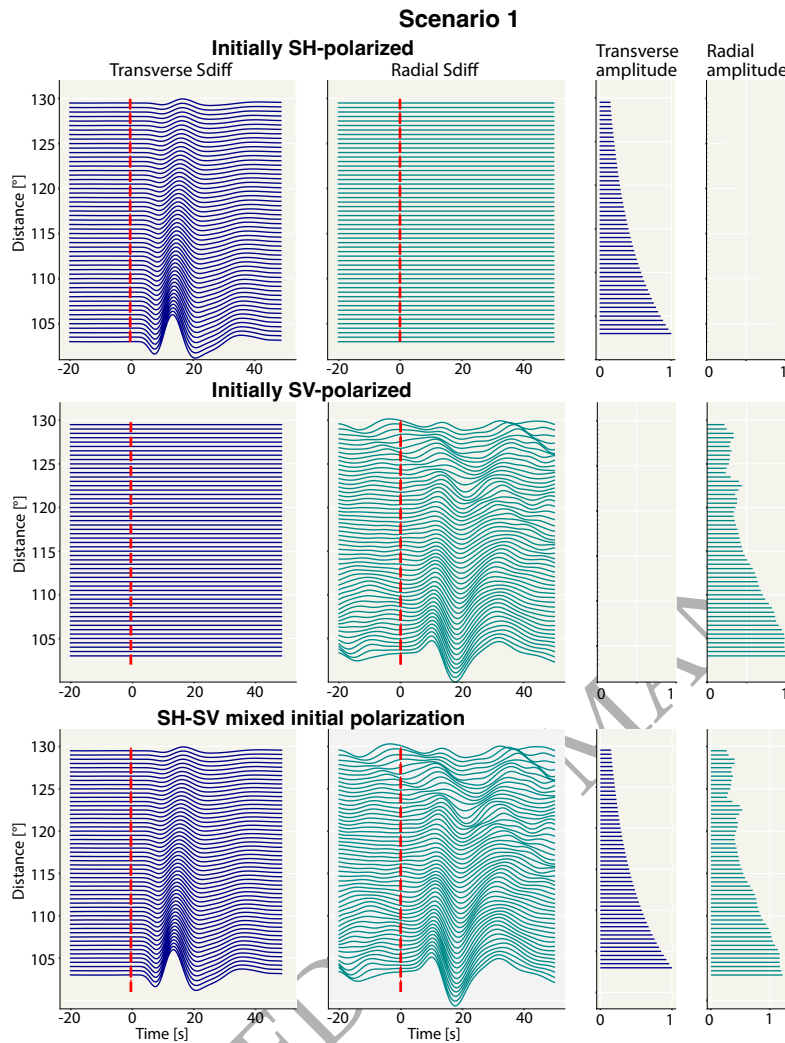


Figure 3: Displacement synthetic seismograms for simulations using PREM (Dziewonski and Anderson, 1981) as an input model (scenario 1 in Figure 2), calculated for a focal depth of 0 km. We show transverse (first column, dark blue) and radial (second column, teal)  $S_{\text{diff}}$  waveforms and corresponding transverse (third column, dark blue) and radial (fourth column, teal) amplitudes as a function of epicentral distance. The amplitudes are plotted relative to the transverse (row 1 and 3) and radial  $S_{\text{diff}}$  (row 2) amplitudes at the lowest distance and measured as the maximum absolute values in a time window of from the predicted  $S_{\text{diff}}$  arrival to 30 s after it. Three simulations are shown for SH (top row), SV (middle row) and mixed SH-SV initial polarizations (bottom row). Seismograms are shown from 20 s before the predicted  $S_{\text{diff}}$  arrival time until 60 s after. Predicted arrival times are calculated using TauP (Crotwell et al., 1999) for the PREM model (red dashed lines). Waveforms are shown after applying a 10 – 50 s bandpass filter.

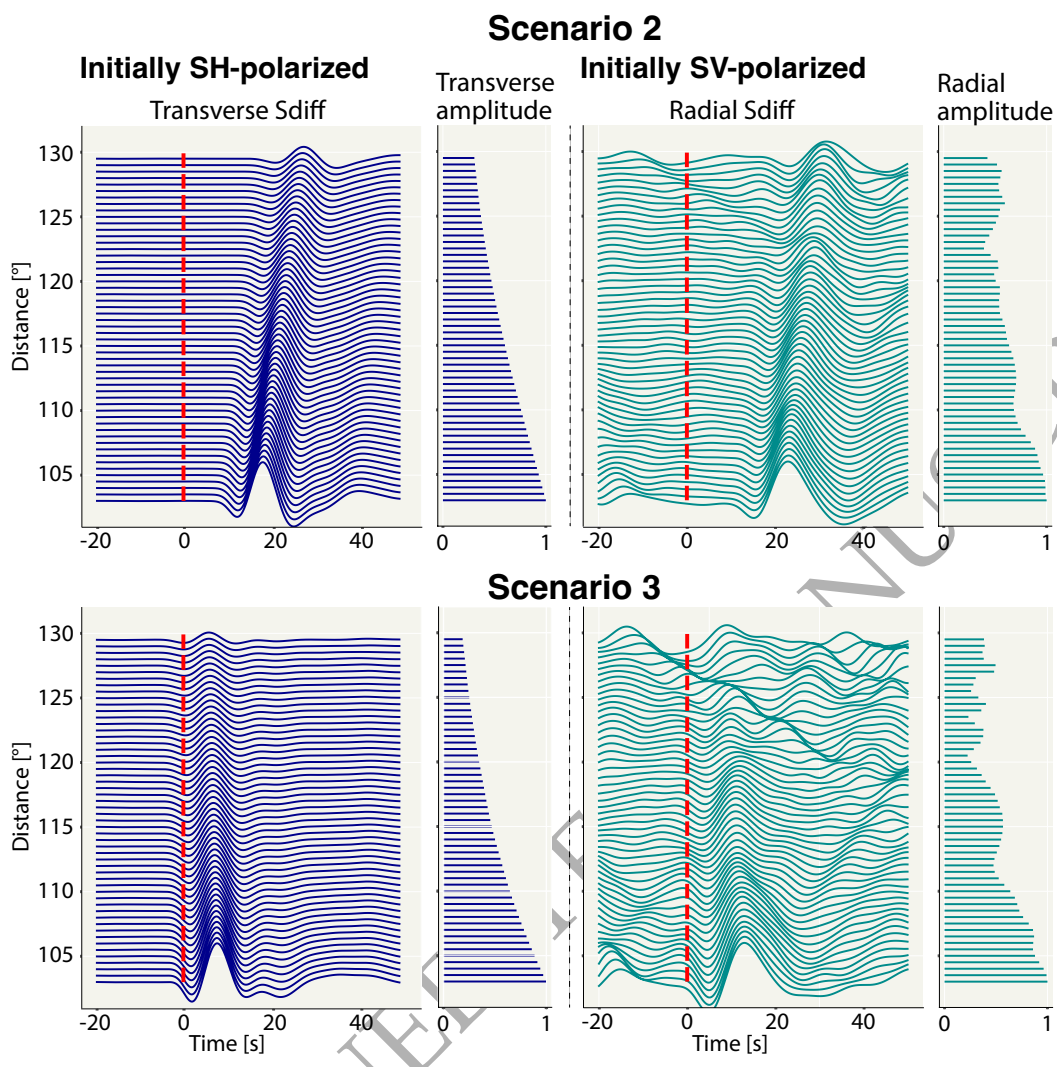


Figure 4: Transverse and radial  $S_{\text{diff}}$  displacement waveforms and amplitudes for 2% lower (scenario 2, top row) and 2% higher (scenario 3, bottom row) shear wave velocities than PREM (Dziewonski and Anderson, 1981) in the lowermost 150 km of the mantle, calculated using a focal depth of 0 km. The amplitudes are plotted relative to the  $SH_{\text{diff}}$  (column 1) and  $SV_{\text{diff}}$  (column 3) amplitudes at the closest distance. Simulations are conducted for initially fully SH (first/second column) and SV (third/fourth column) polarized  $S_{\text{diff}}$  waves. Waveforms are shown in columns 1 and 3; amplitudes are shown in columns 2 and 4. In contrast to Figure 3, only those panels are shown for which  $S_{\text{diff}}$  amplitudes are non-null. Other plotting conventions are the same as in Figure 3.

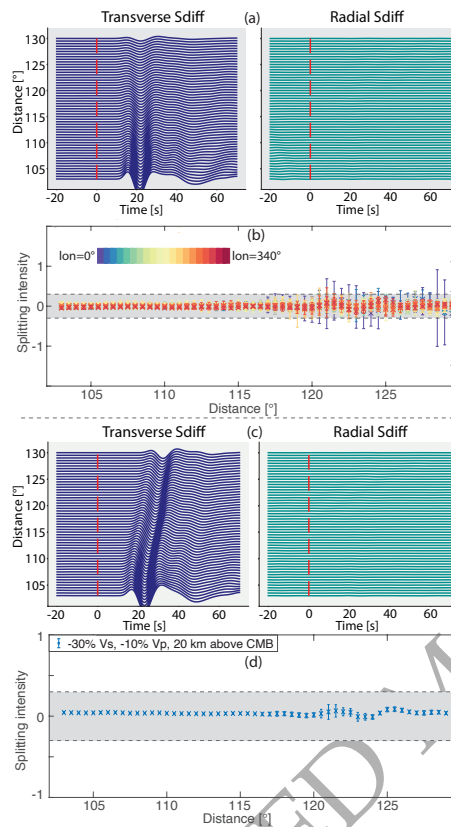


Figure 5: Results from simulations investigating isotropic effects on polarizations of (initially SH polarized)  $S_{\text{diff}}$  waves. (a) Transverse (left panel, dark blue) and radial (right panel, teal) waveforms as a function of distance for a simulation using the 3D tomography model GyPSuM (Simmons et al., 2010) for the mantle and isotropic PREM (Dziewonski and Anderson, 1981) elsewhere, calculated for a focal depth of 0 km. The amplitudes are plotted relative to the transverse  $S_{\text{diff}}$  amplitude at the lowest distance. For this simulation, the source was placed at the north pole and the receivers were positioned along  $60^\circ$  longitude. While a clear arrival is visible on the transverse component, almost no energy arrives on the radial. Red dashed lines indicate predicted arrival times according to PREM. Waveforms are shown after applying a bandpass filter between 10 – 50 s. (b) Splitting intensities, measured using SplitRacer (Reiss and Rmpker, 2017), as a function of distance for analogue source-receiver configurations as in (a), along different longitudes (with a spacing of  $20^\circ$ ; see legend). All splitting intensity measurements are null ( $|SI| < -0.3$ ; indicated by black dashed lines). (c) Results for scenarios that include a global 20 km thick basal layer with largely reduced shear velocities (see legend) are shown. S wave velocity reductions are chosen to be 30% and P wave velocity reduction to be 10% compared to PREM (see legend), which is similar to the velocity reduction expected for ULVZs. (d) Splitting intensities for the scenario shown in c, measured as in panel b.

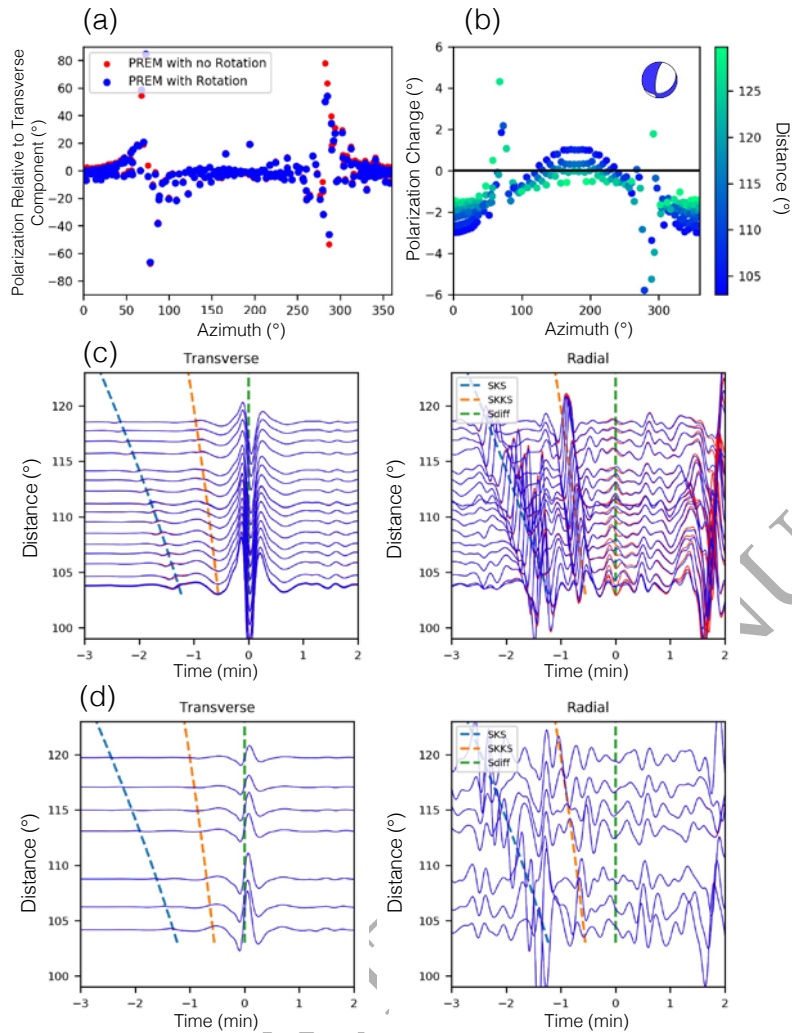


Figure 6: Results for simulations with and without Earth's rotation. (a) Angular deviations of  $S_{\text{diff}}$  polarization from the transverse component for a single, realistic event for isotropic PREM (depth = 616 km), where one simulation includes Earth's rotation (blue) and without (red) using SPEC-FEM3D.GLOBE. (b) The difference in angular deviations for a simulation including Earth's rotation and one without as determined from (a), where each point is colored by arc distance. The event's moment tensor is included at upper right. (c) A small selection of  $S_{\text{diff}}$  waveforms (for azimuths traversing north with an azimuth range of  $340^{\circ}$ - $360^{\circ}$ ) from both simulations for the transverse (left) and radial (right) components (Note: radial waveforms are doubled relative to the transverse component to highlight the difference in waveform shape). Red waveforms represent simulations without Earth's rotation, while blue waveforms include rotation. Predicted PREM arrival times of SKS (light blue), SKKS (orange), and  $S_{\text{diff}}$  (green) are displayed as well. Waveforms are bandpass filtered (10 s-50 s). (d) Another selection of  $S_{\text{diff}}$  waveforms from the same event for azimuths  $100^{\circ}$ - $130^{\circ}$ , plotted with same conventions as (c).

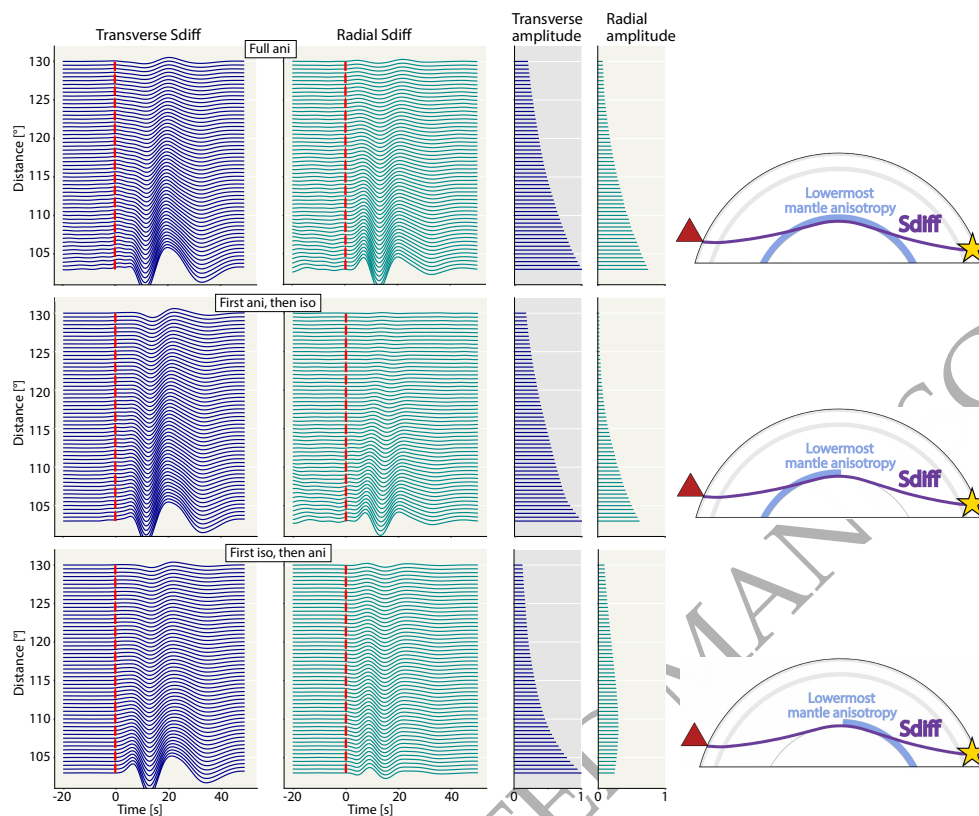


Figure 7: Results from synthetic calculations that use an isotropic PREM (Dziewonski and Anderson, 1981) input model, for which the bottom 150 km of the mantle were replaced by Ppv anisotropy, calculated for a focal depth of 500 km. The initial source polarization is SH for all simulations. (The reason for the difference in waveform shape compared to the previous figures is that we use a slightly different source-receiver configuration here, see Section 2.1). Transverse and radial  $S_{\text{diff}}$  waveforms (columns 1, 2) and corresponding amplitudes (columns 3, 4) are shown for three different cases. The amplitudes are plotted relative to the transverse  $S_{\text{diff}}$  amplitude at the lowest distance. These cases are schematically illustrated in the right column, showing raypaths (violet) from source (yellow star) to receiver (red triangle) for an epicentral distance of  $130^\circ$ , and the location of the lowest mantle anisotropy (light blue). Upper row: full global layer of Ppv anisotropy (represented by light blue color in right column); middle row: lowest mantle anisotropy, incorporated in the deep mantle up to an epicentral distance of  $65^\circ$  measured from the source (see right column); bottom row: lowest mantle anisotropy from an epicentral distance of  $65^\circ$  from the source (see right column). Other plotting conventions are similar to Figure 3.

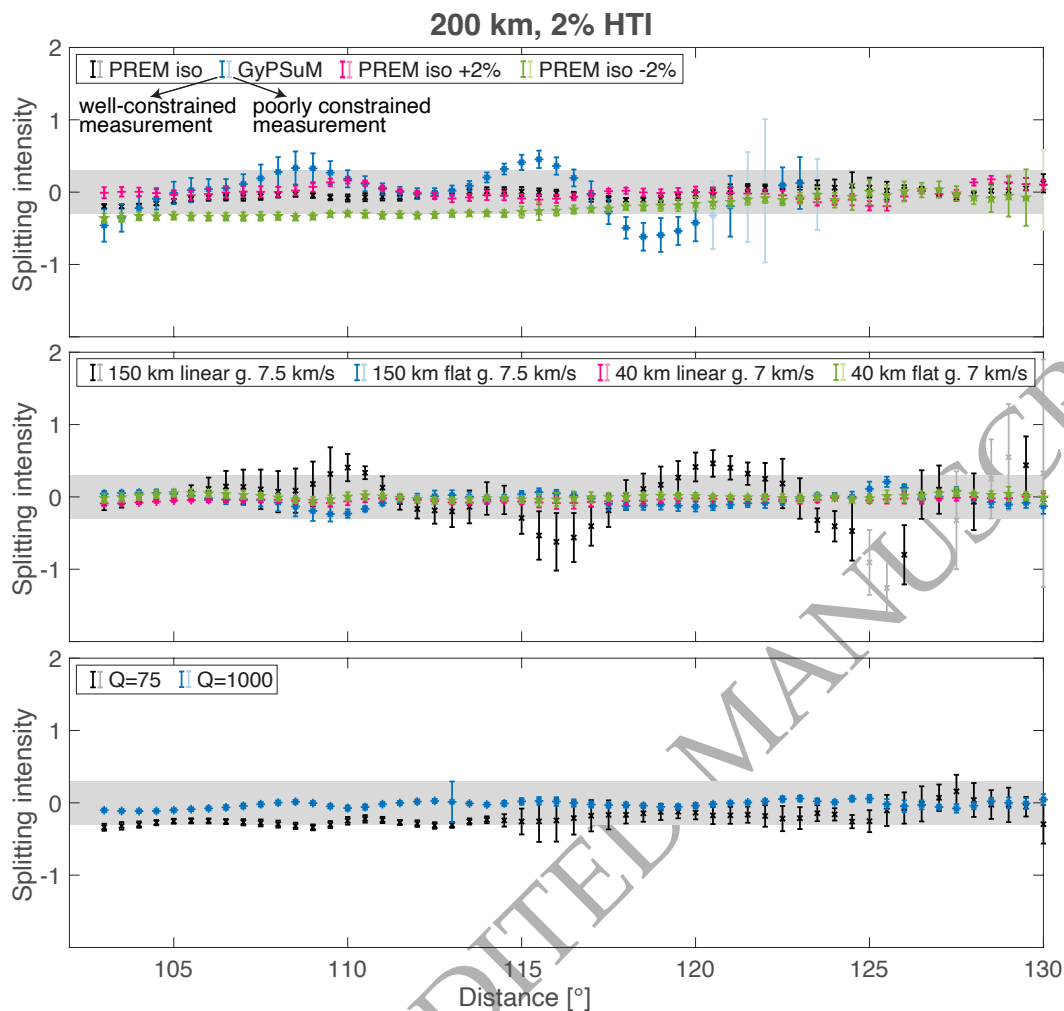


Figure 8: Results from simulations that incorporate only moderate source-side upper mantle anisotropy and no lowermost mantle anisotropy (200 km thick layer, 2% anisotropic strength for an HTI elastic tensor), plotted as  $SH_{\text{diff}}$  splitting intensities as a function of distance, calculated for a focal depth of 500 km.  $SI$  was measured using SplitRacer (Reiss and Rmpker, 2017). 95% confidence intervals are indicated by error bars. Simulations were conducted for all lowermost mantle properties tested in Section 3.1 (see legend). Simulations for which the lowermost mantle velocity was modified are shown in the top panel. These include an input model for which the mantle in PREM has been replaced by the GyPSuM tomographic model (Simmons et al., 2010; see legend). The middle panel shows results for different lowermost mantle velocity gradients, in particular, linear and flat gradients were tested (see legend). The bottom row presents results for two endmember Q-values. The shaded gray area indicates  $SI$ -values between  $-0.3$  and  $0.3$ , which would usually be defined as null. Results for simulations that include strong source-side anisotropy and are identical otherwise are shown in Supplementary Figure S5.

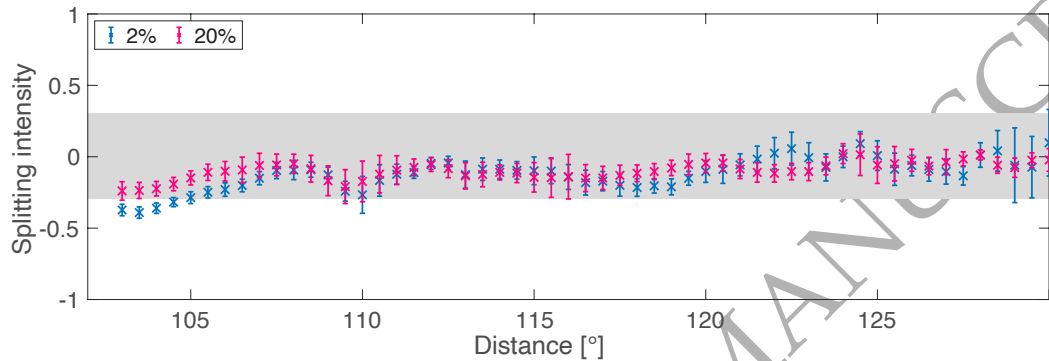


Figure 9: Simulation results, expressed as measured splitting intensities, for initially SH-polarized  $S_{\text{diff}}$  waves for two different velocity reductions at the base of the mantle, in presence of moderately strong source-side upper mantle anisotropy (200 km thick layer, 4% anisotropic strength for an HTI elastic tensor), calculated for a focal depth of 500 km. Plotting conventions are similar to Figure 8. Synthetics were computed for a 20 km thick low velocity layer at the base of the mantle. P wave velocity reductions are 1/3 of the S wave velocity reductions (see legend). 95% confidence intervals are shown by error bars. Almost all of the measurements are null (gray area). Results for other velocity reductions than those shown here are presented in Supplementary Figure S6.

ORIGINAL UNEDITED MANUSCRIPT

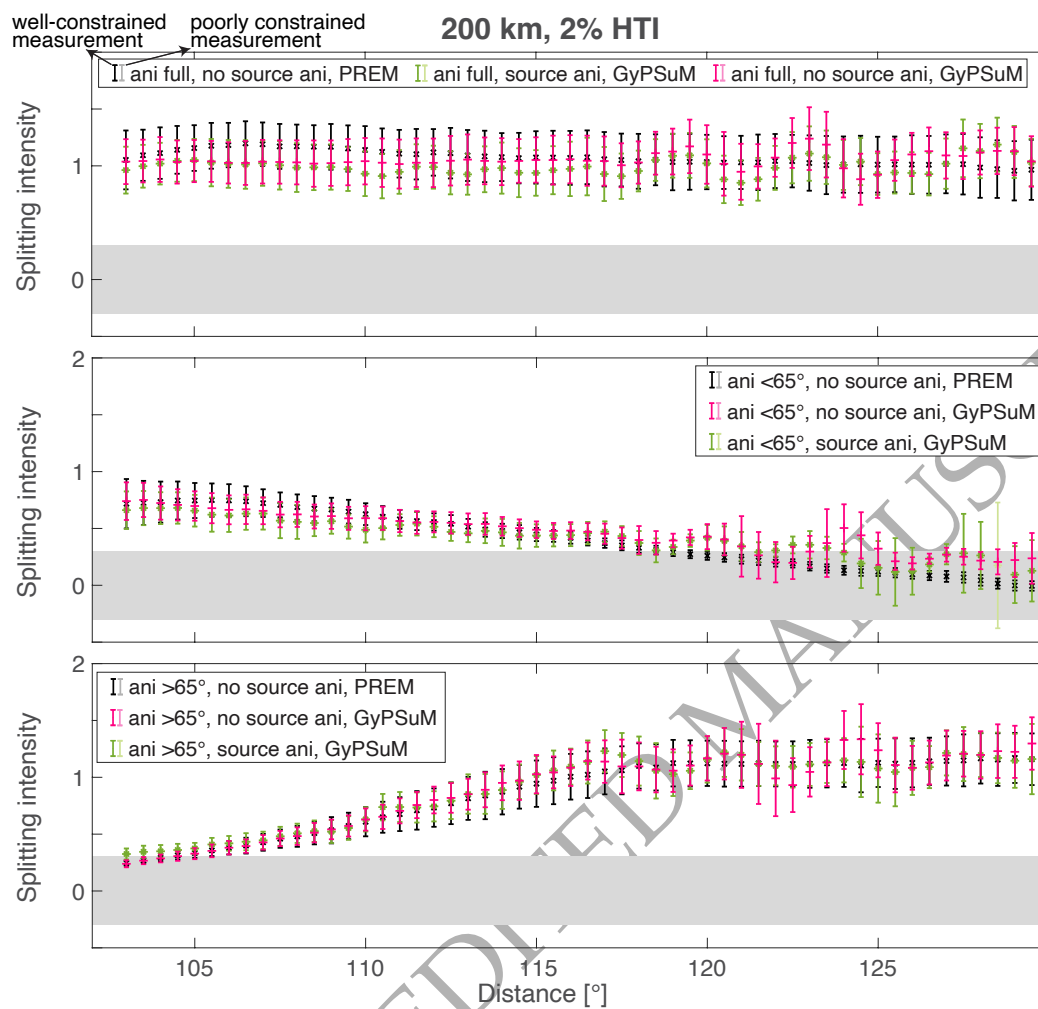


Figure 10: Results for similar scenarios of anisotropy in the lowermost mantle as shown in Figure 7, with similar plotting conventions as in Figure 8. Lowermost mantle anisotropy is incorporated for a full global layer of Ppv anisotropy, up to an epicentral distance of 65° (from the source) or from an epicentral distance of 65° (see legend). All simulations that use an isotropic PREM (Dziewonski and Anderson, 1981) without GyPSuM (Simmons et al., 2010) include lowermost mantle anisotropy only (see legend). Simulations with GyPSuM tomography in the mantle (replacing PREM velocity structure) include source and receiver side anisotropy (see legend). Results are shown for a moderately strongly anisotropic layer (as defined in the caption of Figure 8). Results for simulations that include strong source-side anisotropy and are otherwise identical are shown in Supplementary Figure S5.

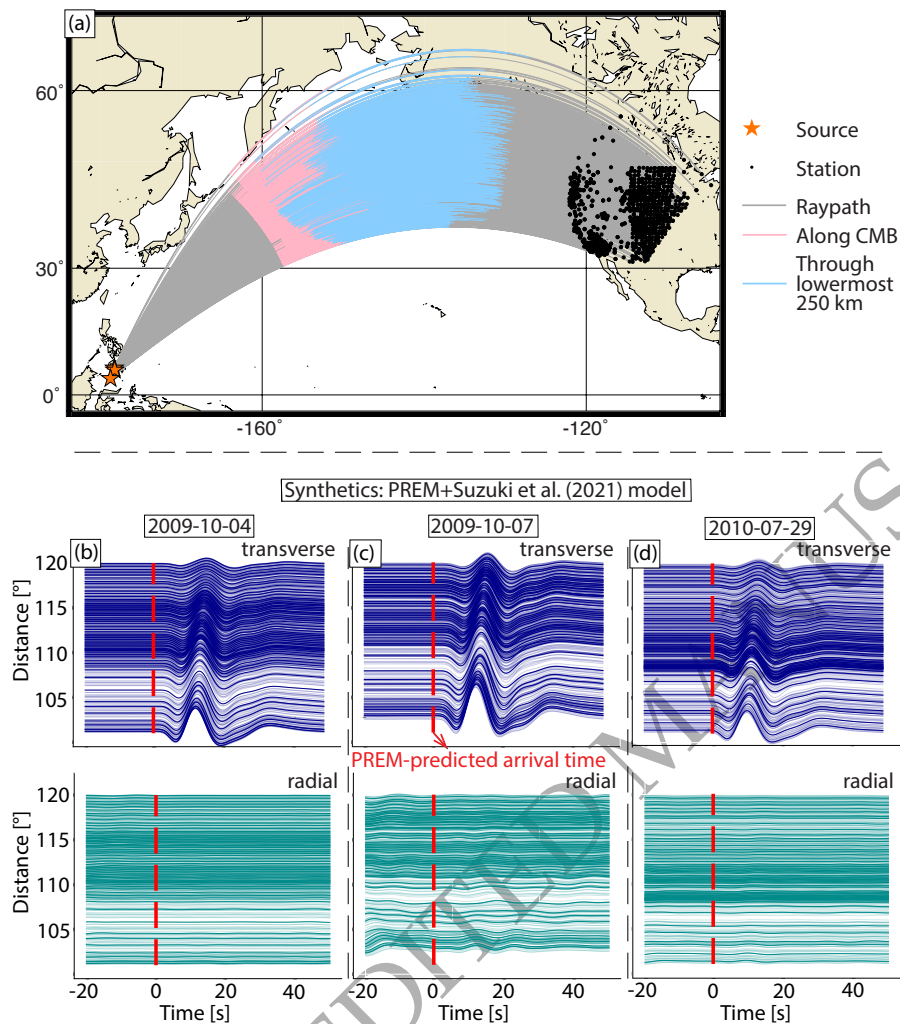


Figure 11: (a) Raypath and station distribution for the  $S_{diff}$  waves used in our real data example. Events are shown as orange stars, stations as black dots.  $S_{diff}$  raypaths for all three events are shown as solid gray lines. The path length along the CMB (pink) and through the lowermost mantle on the receiver side (blue) are emphasized. (b-d) Synthetic displacement seismograms calculated using an isotropic PREM (Dziewonski and Anderson, 1981) input model, for which lowermost mantle velocities have been replaced with an (isotropic) local 3-D velocity model for the lowermost mantle beneath the northern Pacific (Suzuki et al., 2021). Synthetic seismograms for events 2009-10-04 (b), 2009-10-07 (c) and 2010-07-29 (d) are shown as a function of epicentral distance. Seismograms are bandpass-filtered, retaining periods between 8 – 25 s. Transverse components (dark blue) are presented in the top row and radial components (teal) in the bottom row. Predicted  $S_{diff}$  arrival times according to PREM are indicated by red dashed lines. For all three events  $S_{diff}$  is almost fully SH polarized.

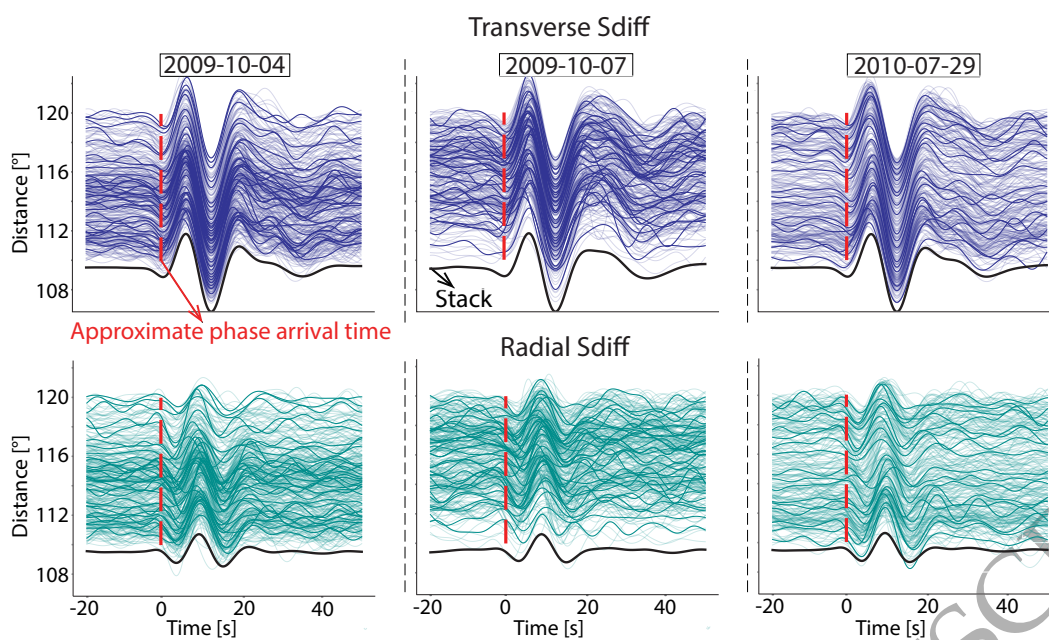


Figure 12: Transverse (top row) and radial (bottom row) component waveforms for the  $S_{\text{diff}}$  waves of all three events (left column: 2009-10-04; middle column: 2009-10-07; right column: 2010-07-29), recorded at a distance  $> 110^\circ$  and an azimuth  $< 43^\circ$  (see text). Waveforms are aligned and normalized with respect to the maximum radial  $S_{\text{diff}}$  amplitudes. Only every 10th trace is plotted without transparency to better visualize the individual waveforms. Red dashed lines represent approximate  $S_{\text{diff}}$  arrival times. Linearly stacked traces are plotted in black color on the corresponding panel.

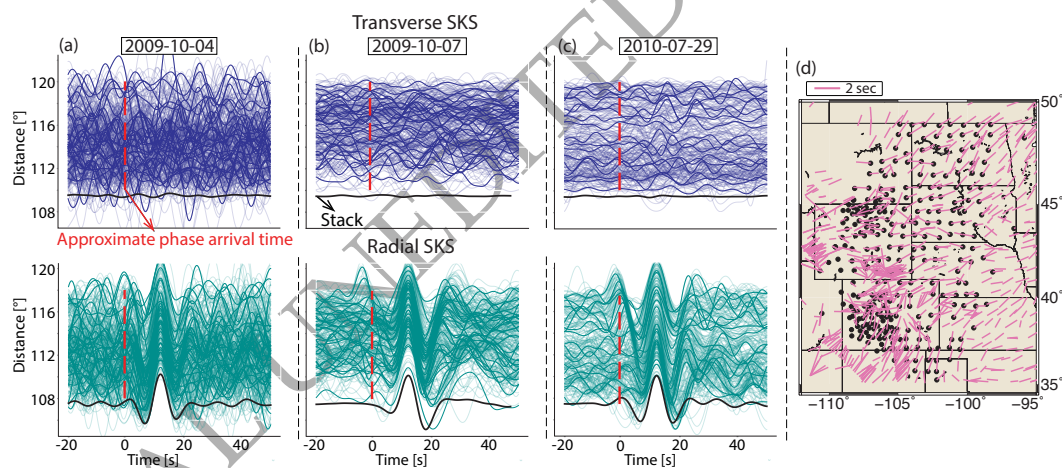


Figure 13: (a-c) SKS waveforms for the same selection of stations and events as in Figure 12. The same plotting conventions as in Figure 12 are used. (d) Zoom-in to the stations (black dots) used for event 2009-10-04. Splitting parameters from the IRIS splitting database (IRIS DMC, 2012) are shown as pink sticks. The orientation of the sticks indicates the fast polarization direction and their length is proportional to the delay time (see legend). Note that the station selection for the two other events is very similar but not identical (e.g., due to different timings of events).

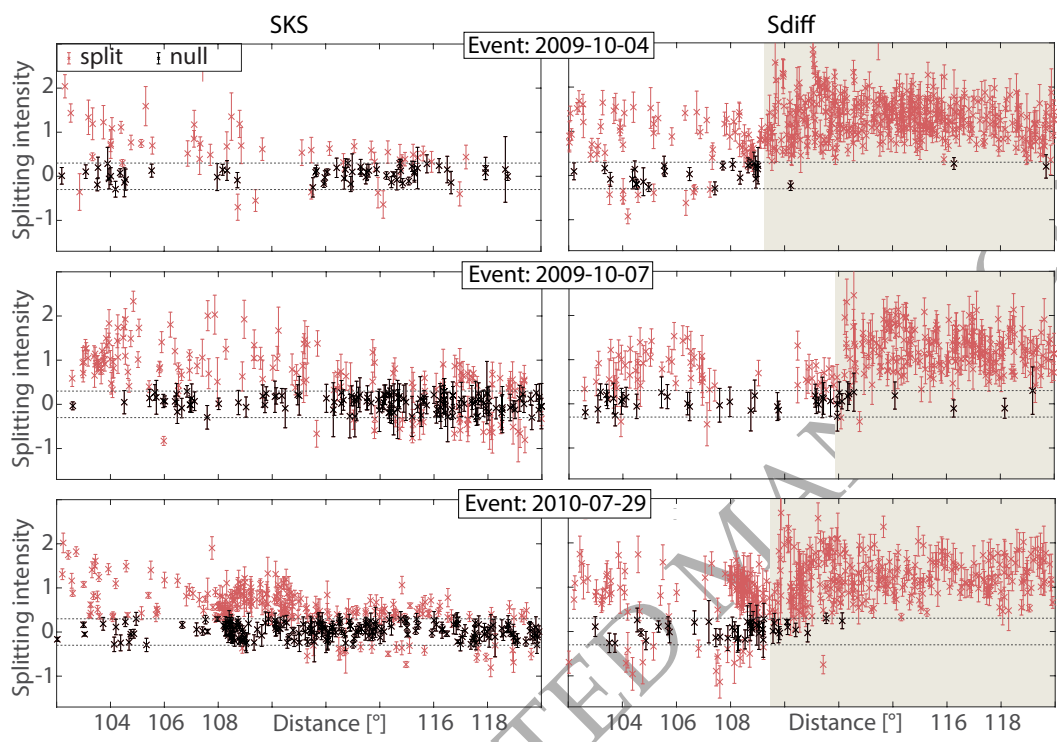


Figure 14: Measurement of splitting intensities for individual seismograms for three events, showing SKS (left column) and  $S_{diff}$  (right column). Top row: for event 2009-10-04; middle row: event 2009-10-07; bottom row: event 2010-07-29. Left column: SKS splitting intensities as a function of distance, measured using SplitRacer (Reiss and Rmpker, 2017). Null results (defined as  $|SI| < 0.3$ ) are plotted in black and split results in red. Error bars indicate 95% confidence intervals. Only high-quality measurements are retained (defined by a 95% confidence interval that is smaller than  $\pm 0.5$ ). Right column:  $S_{diff}$  splitting intensities as a function of distance using the same plotting conventions as for the left row. The area with tan shading indicates the distance range for which particularly strong  $S_{diff}$  splitting can be observed for each event.

ORIGINAL UNEDITED MANUSCRIPT

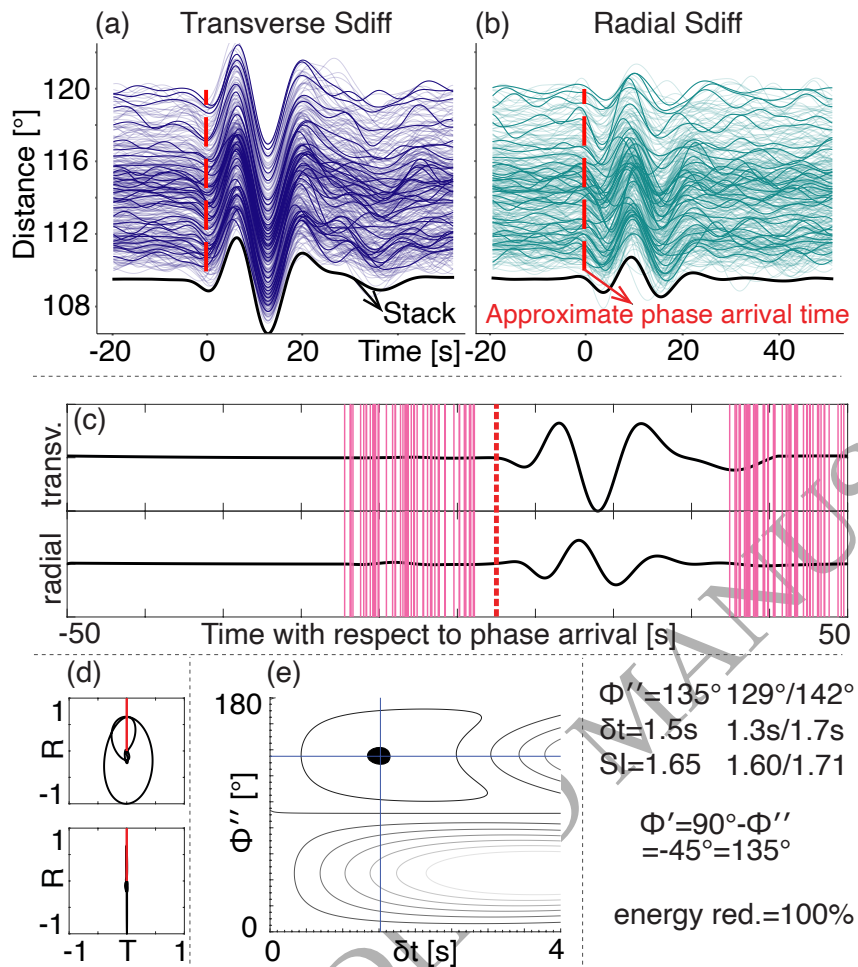


Figure 15:  $S_{\text{diff}}$  waveforms and splitting diagnostic plots from SplitRacer (Reiss and Rmpker, 2017) for event 2009-10-04. Similar plots for the other two events are shown in Supplementary Figures S11 and S12. In the waveform plots, approximate  $S_{\text{diff}}$  arrival times as are shown as a red dashed lines. (a) Transverse component waveforms recorded at a distance  $> 110^{\circ}$  and an azimuth  $< 43^{\circ}$  (see text). Waveforms were aligned and normalized with respect to the maximum transverse  $S_{\text{diff}}$  amplitudes. (b) Similar representation of the corresponding radial  $S_{\text{diff}}$  waveforms. Only every 10th trace is plotted without transparency to better visualize the individual waveforms. (c) Waveforms of the  $S_{\text{diff}}$  stack (radial, top trace; transverse, bottom trace) are shown as black solid lines and the start/end of the 50 randomly chosen measurement windows as pink lines. (d) The upper diagram shows the particle motion for the original stack, the lower diagrams for the waveforms that were corrected for splitting. The red lines in the diagrams indicate the backazimuthal direction. (e) The best fitting splitting parameters are shown in the  $\phi'' - \delta t$ -plane, with black color indicating the 95% confidence region. For an explanation of the splitting parameters  $\phi''$  and  $\phi'$  see Section 2.2.

- Backus, G., Gilbert, F., 1961. The rotational splitting of the free oscillations of the earth. *Proceedings of the National Academy of Sciences of the United States of America* 47 (3), 362.
- Barruol, G., Kern, H., 1996. Seismic anisotropy and shear-wave splitting in lower-crustal and upper-mantle rocks from the Ivrea Zone: experimental and calculated data. *Physics of the Earth and Planetary Interiors* 95, 175–194.  
URL [https://doi.org/10.1016/0031-9201\(95\)03124-3](https://doi.org/10.1016/0031-9201(95)03124-3)
- Becker, T. W., Schaeffer, A. J., Lebedev, S., Conrad, C. P., 2015. Toward a generalized plate motion reference frame. *Geophysical Research Letters* 42 (9), 3188 – 3196.  
URL <https://doi.org/10.1002/2015GL063695>
- Beyreuther, M., Barsch, R., Krischer, L., Megies, T., Behr, Y., Wassermann, J., 06 2010. Obspy: A python toolbox for seismology. *Seismological Research Letters* 81, 530–533.  
URL <https://doi.org/10.1111/10.1785/gssr1.81.3.530>
- Borgeaud, A. F., Konishi, K., Kawai, K., Geller, R. J., 2016. Finite frequency effects on apparent S-wave splitting in the D layer: comparison between ray theory and full-wave synthetics. *Geophysical Journal International* 207, 12–28.  
URL <https://doi.org/10.1093/gji/ggw254>
- Chang, S.-J., Ferreira, A. M., Ritsema, J., van Heijst, H. J., Woodhouse, J. H., 2014. Global radially anisotropic mantle structure from multiple datasets: A review, current challenges, and outlook. *Tectonophysics* 617, 1–19.  
URL <https://doi.org/10.1016/j.tecto.2014.01.033>
- Chang, S.-J., Ferreira, A. M. G., 2019. Inference on Water Content in the Mantle Transition Zone Near Subducted Slabs From Anisotropy Tomography. *Geochemistry, Geophysics, Geosystems* 20, 1189–1201.  
URL <https://doi.org/10.1029/2018GC008090>
- Chevrot, S., 2000. Multichannel analysis of shear wave splitting. *Journal of Geophysical Research: Solid Earth* 105, 21579–21590.  
URL <https://doi.org/10.1029/2000JB900199>
- Cottaar, S., Romanowicz, B., 2013. Observations of changing anisotropy across the southern margin of the African LLSVP. *Geophysical Journal International* 195, 1184–1195.  
URL <https://doi.org/10.1093/gji/ggt285>
- Creasy, N., Bozdag, E., Frost, D. A., Snieder, R., in review. Body Wave Polarization Anomalies due to Earths Coriolis Effect.

- Creasy, N., Long, M. D., Ford, H. A., 2017. Deformation in the lowermost mantle beneath Australia from observations and models of seismic anisotropy. *Journal of Geophysical Research: Solid Earth* 122, 5243–5267.  
URL <https://doi.org/10.1002/2016JB013901>
- Creasy, N., Miyagi, L., Long, M. D., 2020. A Library of Elastic Tensors for Lowermost Mantle Seismic Anisotropy Studies and Comparison With Seismic Observations. *Geochemistry, Geophysics, Geosystems* 21, e2019GC008883.  
URL <https://doi.org/10.1029/2019GC008883>
- Creasy, N., Pisconti, A., Long, M. D., Thomas, C., 2021. Modeling of Seismic Anisotropy Observations Reveals Plausible Lowermost Mantle Flow Directions Beneath Siberia. *Geochemistry, Geophysics, Geosystems* 22 (10), e2021GC009924.  
URL <https://doi.org/10.1029/2021GC009924>
- Creasy, N., Pisconti, A., Long, M. D., Thomas, C., Wookey, J., 2019. Constraining lowermost mantle anisotropy with body waves: A synthetic modelling study. *Geophysical Journal International* 217 (2), 766–783.
- Crotwell, P., Owens, T. J., Ritsema, J., 1999. The TauP Toolkit: Flexible Seismic Travel-Time and Raypath Utilities. *Seismological Research Letters* 70.  
URL <https://doi.org/10.1785/gssr1.70.2.154>
- Dahlen, F. A., Tromp, J., 1998. *Theoretical Global Seismology*. Princeton University Press.
- Doornbos, D. J., Mondt, J. C., 1979. Attenuation of P and S waves diffracted around the core. *Geophysical Journal International* 57 (2), 353–379.  
URL <https://doi.org/10.1111/j.1365-246X.1979.tb04783.x>
- Dziewonski, A. M., Anderson, D. L., 1981. Preliminary reference Earth model. *Physics of the Earth and Planetary Interiors* 25, 297–356.  
URL [https://doi.org/10.1016/0031-9201\(81\)90046-7](https://doi.org/10.1016/0031-9201(81)90046-7)
- Ekström, G., Nettles, M., Dziewoński, A., 2012. The global cmt project 2004–2010: Centroid-moment tensors for 13,017 earthquakes. *Physics of the Earth and Planetary Interiors* 200, 1–9.  
URL <https://doi.org/10.1016/j.pepi.2012.04.002>
- Erdman, M. E., Hacker, B. R., Zandt, G., Seward, G., 2013. Seismic anisotropy of the crust: electron-backscatter diffraction measurements from the Basin and Range. *Geophysical Journal International* 195, 1211–1229.  
URL <https://doi.org/10.1093/gji/ggt287>

- Ferreira, A., Faccenda, M., Sturgeon, W., Chang, S.-J., Schardong, L., 2019. Ubiquitous lower-mantle anisotropy beneath subduction zones. *Nature Geoscience* 12, 301–306.  
URL <https://doi.org/10.1038/s41561-019-0325-7>
- Foley, B. J., Long, M. D., 2011. Upper and mid-mantle anisotropy beneath the Tonga slab. *Geophysical Research Letters* 38.  
URL <https://doi.org/10.1029/2010GL046021>
- Ford, H. A., Long, M. D., He, X., Lynner, C., 2015. Lowermost mantle flow at the eastern edge of the African Large Low Shear Velocity Province. *Earth and Planetary Science Letters* 420, 12–22.  
URL <https://doi.org/10.1016/j.epsl.2015.03.029>
- Fouch, M. J., Fischer, K. M., Wysession, M. E., 2001. Lowermost mantle anisotropy beneath the Pacific: Imaging the source of the Hawaiian plume. *Earth and Planetary Science Letters* 190 (3), 167–180.  
URL [https://doi.org/10.1016/S0012-821X\(01\)00380-6](https://doi.org/10.1016/S0012-821X(01)00380-6)
- French, S. W., Romanowicz, B. A., 2014. Whole-mantle radially anisotropic shear velocity structure from spectral-element waveform tomography. *Geophysical Journal International* 199 (3), 1303–1327.  
URL <https://doi.org/10.1093/gji/ggu334>
- Frost, D. A., Lasbleis, M., Chandler, B., Romanowicz, B., 2021. Dynamic history of the inner core constrained by seismic anisotropy. *Nature Geoscience*, 531–535.  
URL <https://doi.org/10.1038/s41561-021-00761-w>
- Garnero, E. J., Lay, T., 1997. Lateral variations in lowermost mantle shear wave anisotropy beneath the north Pacific and Alaska. *Journal of Geophysical Research: Solid Earth* 102 (B4), 8121–8135.  
URL <https://doi.org/10.1029/96JB03830>
- Garnero, E. J., Moore, M. M., Lay, T., Fouch, M. J., 2004. Isotropy or weak vertical transverse isotropy in D" beneath the Atlantic Ocean. *Journal of Geophysical Research: Solid Earth* 109 (B8), 1–10.  
URL <https://doi.org/10.1029/2004JB003004>
- IRIS DMC, 2012. Data Services Products: SWS-DBs Shear-wave splitting databases.  
URL <https://doi.org/10.17611/DP/SWS.1>
- IRIS Transportable Array, 2003. USArray Transportable Array.  
URL <https://www.fdsn.org/networks/detail/TA/>

- Karato, S.-I., Jung, H., Katayama, I., Skemer, P., 2008. Geodynamic Significance of Seismic Anisotropy of the Upper Mantle: New Insights from Laboratory Studies. *Annual Review of Earth and Planetary Sciences* 36, 59–95.  
URL <https://doi.org/10.1146/annurev.earth.36.031207.124120>
- Komatitsch, D., Tromp, J., 2002a. Spectral-element simulations of global seismic wave propagation I. Validation. *Geophysical Journal International* 149 (2), 390–412.  
URL <https://doi.org/10.1046/j.1365-246X.2002.01653.x>
- Komatitsch, D., Tromp, J., 2002b. Spectral-element simulations of global seismic wave propagation II. Three-dimensional models, oceans, rotation and self-gravitation. *Geophysical Journal International* 150 (1), 303–318.  
URL <https://doi.org/10.1046/j.1365-246X.2002.01716.x>
- Komatitsch, D., Vinnik, L. P., Chevrot, S., 2010. SHdiff-SVdiff splitting in an isotropic Earth. *Journal of Geophysical Research: Solid Earth* 115 (B7).  
URL <https://doi.org/10.1029/2009JB006795>
- Lawrence, J. F., Wyssession, M. E., 2006. QLM9: A new radial quality factor (Q) model for the lower mantle. *Earth and Planetary Science Letters* 241 (3), 962–971.  
URL <https://doi.org/10.1016/j.epsl.2005.10.030>
- Lay, T., Williams, Q., Garnero, E. J., Kellogg, L., Wyssession, M. E., 1998. Seismic Wave Anisotropy in the D Region and Its Implications. *American Geophysical Union (AGU)*, pp. 299–318.  
URL <https://doi.org/10.1029/GD028p0299>
- Leng, K., Nissen-Meyer, T., van Driel, M., 2016. Efficient global wave propagation adapted to 3-D structural complexity: a pseudospectral/spectral-element approach. *Geophysical Journal International* 207 (3), 1700–1721.  
URL <https://doi.org/10.1093/gji/ggw363>
- Leng, K., Nissen-Meyer, T., van Driel, M., Hosseini, K., Al-Attar, D., 2019. AxiSEM3D: broad-band seismic wavefields in 3-D global earth models with undulating discontinuities. *Geophysical Journal International* 217 (3), 2125–2146.  
URL <https://doi.org/10.1093/gji/ggz092>
- Long, M. D., Becker, T., 2010. Mantle dynamics and seismic anisotropy. *Earth and Planetary Science Letters* 297, 341–354.  
URL <https://doi.org/10.1016/j.epsl.2010.06.036>

- Long, M. D., Silver, P. G., 2009. Shear Wave Splitting and Mantle Anisotropy: Measurements, Interpretations, and New Directions. *Surveys in Geophysics* 30, 407–461.  
URL <https://doi.org/10.1007/s10712-009-9075-1>
- Lutz, K., Long, M., Creasy, N., Deng, J., 2020. Seismic anisotropy in the lowermost mantle beneath North America from SKS-SKKS splitting intensity discrepancies. *Physics of the Earth and Planetary Interiors* 305, 106504.  
URL <https://doi.org/10.1016/j.pepi.2020.106504>
- Lynner, C., Long, M. D., 2014. Lowermost mantle anisotropy and deformation along the boundary of the African LLSVP. *Geophysical Research Letters*, 3447–3454.  
URL <https://doi.org/10.1002/2014GL059875>
- Lynner, C., Long, M. D., 2015. Heterogeneous seismic anisotropy in the transition zone and uppermost lower mantle: evidence from South America, Izu-Bonin and Japan. *Geophysical Journal International* 201, 1545–1552.  
URL <https://doi.org/10.1093/gji/ggv099>
- Masters, G., Park, J., Gilbert, F., 1983. Observations of coupled spheroidal and toroidal modes. *Journal of Geophysical Research: Solid Earth* 88 (B12), 10285–10298.  
URL <https://doi.org/10.1029/JB088iB12p10285>
- Mohiuddin, A., D. Long, M., Lynner, C., 2015. Mid-mantle seismic anisotropy beneath Southwestern Pacific subduction systems and implications for mid-mantle deformation. *Physics of the Earth and Planetary Interiors* 245.  
URL <https://doi.org/10.1016/j.pepi.2015.05.003>
- Nowacki, A., Wookey, J., 2016. The limits of ray theory when measuring shear wave splitting in the lowermost mantle with ScS waves. *Geophysical Journal International* 207, 1573–1583.  
URL <https://doi.org/10.1093/gji/ggw358>
- Nowacki, A., Wookey, J., Kendall, J.-M., 2010. Deformation of the lowermost mantle from seismic anisotropy. *Nature* 467, 1091–1094.  
URL <https://doi.org/10.1038/nature09507>
- Nowacki, A., Wookey, J., Kendall, J.-M., 2011. New advances in using seismic anisotropy, mineral physics and geodynamics to understand deformation in the lowermost mantle. *Journal of Geodynamics* 52, 205–228.  
URL <https://doi.org/10.1016/j.jog.2011.04.003>

- Panning, M., Romanowicz, B., 2006. A three-dimensional radially anisotropic model of shear velocity in the whole mantle. *Geophysical Journal International* 167, 361–379.  
URL <https://doi.org/10.1111/j.1365-246X.2006.03100.x>
- Parisi, L., Ferreira, A. M. G., Ritsema, J., 2018. Apparent Splitting of S Waves Propagating Through an Isotropic Lowermost Mantle. *Journal of Geophysical Research: Solid Earth* 123, 3909–3922.  
URL <https://doi.org/10.1002/2017JB014394>
- Park, J., Gilbert, F., 1986. Coupled free oscillations of an aspherical, dissipative, rotating earth: Galerkin theory. *Journal of Geophysical Research: Solid Earth* 91 (B7), 7241–7260.
- Reiss, M., Rmpker, G., 2017. SplitRacer: MATLAB Code and GUI for Semiautomated Analysis and Interpretation of Teleseismic ShearWave Splitting. *Seismological Research Letters* 88, 392 – 409.  
URL <https://doi.org/10.1785/0220160191>
- Reiss, M. C., Long, M. D., Creasy, N., 2019. Lowermost Mantle Anisotropy Beneath Africa From Differential SKS-SKKS Shear-Wave Splitting. *Journal of Geophysical Research: Solid Earth* 124 (8), 8540–8564.  
URL <https://doi.org/10.1029/2018JB017160>
- Ritsema, J., Deuss, A., van Heijst, H. J., Woodhouse, J. H., 2011. S40RTS: a degree-40 shear-velocity model for the mantle from new Rayleigh wave dispersion, teleseismic traveltimes and normal-mode splitting function measurements. *Geophysical Journal International* 184 (3), 1223–1236.  
URL <https://doi.org/10.1111/j.1365-246X.2010.04884.x>
- Ritsema, J., Lay, T., Garnero, E., Benz, H., 1998. Seismic anisotropy in the lowermost mantle beneath the Pacific. *Geophysical Research Letters* 25, 1229–1232.  
URL <https://doi.org/10.1029/98GL00913>
- Romanowicz, B., Cao, A., Godwal, B., Wenk, R., Ventosa, S., Jeanloz, R., 2016. Seismic anisotropy in the Earth's innermost inner core: Testing structural models against mineral physics predictions. *Geophysical Research Letters* 43 (1), 93 – 100.  
URL <https://doi.org/10.1002/2015GL066734>
- Romanowicz, B., Mitchell, B., 2007. Deep Earth Structure -Q of the Earth from Crust to Core. *Treatise on Geophysics*, 731–774.  
URL <https://doi.org/10.1016/B978-044452748-6.00024-9>

- Russo, R., Gallego, A., Comte, D., Mocanu, V., Murdie, R., VanDecar, J., 2010. Source-side shear wave splitting and upper mantle flow in the Chile Ridge subduction Region. *Geology* 38, 707–710.  
URL <https://doi.org/10.1130/G30920.1>
- Schoenberg, M., Censor, D., 1973. Elastic waves in rotating media. *Quarterly of Applied Mathematics* 31 (1), 115–125.
- Silver, P. G., 1996. Seismic Anisotropy beneath the Continents: Probing the Depths of Geology. *Annual Review of Earth and Planetary Sciences* 24 (1), 385 – 432.  
URL <https://doi.org/10.1146/annurev.earth.24.1.385>
- Silver, P. G., Chan, W. W., 1991. Shear wave splitting and subcontinental mantle deformation. *Journal of Geophysical Research: Solid Earth* 96, 16429–16454.  
URL <https://doi.org/10.1029/91JB00899>
- Simmons, N. A., Forte, A. M., Boschi, L., Grand, S. P., 2010. GyPSuM: A joint tomographic model of mantle density and seismic wave speeds. *Journal of Geophysical Research: Solid Earth* 115.  
URL <https://doi.org/10.1029/2010JB007631>
- Snieder, R., Sens-Schönfelder, C., 2021. Local coupling and conversion of surface waves due to earths rotation. part 1: theory. *Geophysical Journal International* 225 (1), 158–175.
- Snieder, R., Sens-Schönfelder, C., Ruigrok, E., Shiomi, K., 2016. Seismic shear waves as focault pendulum. *Geophysical Research Letters* 43 (6), 2576–2581.
- Stackhouse, S., Brodholt, J. P., Wookey, J., Kendall, J.-M., Price, G. D., 2005. The effect of temperature on the seismic anisotropy of the perovskite and post-perovskite polymorphs of MgSiO<sub>3</sub>. *Earth and Planetary Science Letters* 230, 1–10.
- Suzuki, Y., Kawai, K., Geller, R., 2021. Imaging paleoslabs and inferring the Clapeyron slope in D" beneath the northern Pacific based on high-resolution inversion of seismic waveforms for 3-D transversely isotropic structure. *Physics of the Earth and Planetary Interiors* 321, 106751.  
URL <https://doi.org/10.1016/j.pepi.2021.106751>
- Tesoniero, A., Leng, K., D.Long, M., Nissen-Meyer, T., 2020. Full wave sensitivity of SK(K)S phases to arbitrary anisotropy in the upper and lower mantle. *Geophysical Journal International* 222 (1), 412 – 435.  
URL <https://doi.org/10.1093/gji/ggaa171>

- Towns, J., Cockerill, T., Dahan, M., Foster, I., Gaither, K., Grimshaw, A., Hazlewood, V., Lathrop, S., Lifka, D., Peterson, G. D., et al., 2014. Xsede: accelerating scientific discovery. *Computing in science & engineering* 16 (5), 62–74.
- Tromp, J., 1994. Surface-wave propagation on a rotating, anisotropic earth. *Geophysical Journal International* 117 (1), 141–152.
- Vinnik, L., Breger, L., Romanowicz, B., 1998a. Anisotropic structures at the base of the Earth's mantle. *Nature* 393, 564–567.
- Vinnik, L., Brger, L., Romanowicz, B., 1998b. On the inversion of Sd particle motion for seismic anisotropy in D'. *Geophysical Research Letters* 25 (5), 679–682.  
URL <https://doi.org/10.1029/98GL00190>
- Vinnik, L., Farra, V., Romanowicz, B., 1989. Observational evidence for diffracted SV in the shadow of the Earth's core. *Geophysical Research Letters - GEOPHYS RES LETT* 16, 519–522.  
URL <https://doi.org/GL016i006p00519>
- Vinnik, L., Romanowicz, B., Le Stunff, Y., Makeyeva, L., 1995. Seismic anisotropy in the D" layer. *Geophysical Research Letters* 22 (13), 1657–1660.  
URL <https://doi.org/10.1029/95GL01327>
- Walker, A., Wookey, J., 2012. MSAT - a new toolkit for the analysis of elastic and seismic anisotropy. *Computers and Geosciences* 49, 81–90.  
URL <https://doi.org/10.1016/j.cageo.2012.05.031>
- Walsh, E., Arnold, R., Savage, M. K., 2013. Silver and Chan revisited. *Journal of Geophysical Research: Solid Earth* 118, 5500–5515.  
URL <https://doi.org/10.1002/jgrb.50386>
- Wessel, P., Smith, W. H. F., 1998. New, improved version of generic mapping tools released. *Eos, Transactions American Geophysical Union* 79, 579–579.  
URL <https://doi.org/10.1029/98E000426>
- Wolf, J., Creasy, N., Pisconti, A., Long, M. D., Thomas, C., 2019. An investigation of seismic anisotropy in the lowermost mantle beneath Iceland. *Geophysical Journal International* 219 (Supplement<sub>1</sub>), S152 – –S166.  
URL
- Wolf, J., Frost, D. A., Long, M. D., Ganero, E., Aderoju, A. O., Creasy, N., Bozdog, E., 2022. Observations of mantle seismic anisotropy using array techniques: shear-wave splitting

- of beamformed SmKS phases. *Earth and Space Science Open Archive*, 43.  
<https://doi.org/10.1002/essoar.10512340.1>
- Wolf, J., Long, M. D., 2022. Slab-driven flow at the base of the mantle beneath the north-eastern pacific ocean. *Earth and Planetary Science Letters* 594, 117758.  
<https://doi.org/10.1016/j.epsl.2022.117758>
- Wolf, J., Long, M. D., Leng, K., Nissen-Meyer, T., 2022a. Constraining deep mantle anisotropy with shear wave splitting measurements: Challenges and new measurement strategies. *Geophysical Journal International* 230, 507–527.  
<https://doi.org/10.1093/gji/ggac055>
- Wolf, J., Long, M. D., Leng, K., Nissen-Meyer, T., 2022b. Sensitivity of SK(K)S and ScS phases to heterogeneous anisotropy in the lowermost mantle from global wavefield simulations. *Geophysical Journal International* 228, 366–386.  
<https://doi.org/10.1093/gji/ggab347>
- Wookey, J., Kendall, J.-M., Rümpker, G., 2005. Lowermost mantle anisotropy beneath the north Pacific from differential S-ScS splitting. *Geophysical Journal International* 161, 829–838.  
<https://doi.org/10.1111/j.1365-246X.2005.02623.x>
- Yu, S., Garnero, E. J., 2018. Ultralow Velocity Zone Locations: A Global Assessment. *Geochemistry, Geophysics, Geosystems*.  
<https://doi.org/10.1002/2017GC007281>
- Yuan, K., Beghein, C., 2014. Three-dimensional variations in Love and Rayleigh wave azimuthal anisotropy for the upper 800km of the mantle. *Journal of Geophysical Research: Solid Earth* 119, 3232–3255.  
<https://doi.org/10.1002/2013JB010853>